STEMedicine

Vol 2 • Issue 7 • Jul 2021

ISSN 2705-1188

Mechanisms linking hyperglycemia in pregnancy to the offspring cardiovascular system dysfunction

STEMedicine

stemedicine.org

REVIEW ARTICLE

Mechanisms linking hyperglycemia in pregnancy to cardiovascular system dysfunction in offspring

Zemeng XIAO[1], Yifan WANG[1], Phung N. THAI[2], Xuxia LI[1], Xiyuan LU[1,*], Jun PU[1,*],

[1] *State Key Laboratory for Oncogenes and Related Genes, Division of Cardiology, Renji Hospital, School of Medicine, Shanghai Cancer Institute, Shanghai Jiaotong University, Shanghai, China.*
[2] *Department of Internal Medicine, Cardiology, University of California, Davis.*

*Correspondence: pjrenji@163.com, luxiyuan2020@126.com
https://doi.org/10.37175/stemedicine.v2i7.91

ABSTRACT

Hyperglycemia in pregnancy (HIP) is a high-glycemic state that occurs during pregnancy, and gestational diabetes mellitus (GDM) is the major cause of it. Studies reveal that GDM has long-term adverse impacts on mothers and offspring, such as maternal type 2 diabetes, premature birth and stillbirth in newborns, cardiovascular disease, and metabolic disorders in adult offspring. In recent years, studies on the transcription level of GDM and metabonomics have provided new insights into the pathophysiological mechanism of GDM. This article reviews the transcriptional levels and metabolomics studies involving GDM and cardiovascular dysfunction in the offspring, which may provide insight to the long-term health of pregnant women and offspring.

Keywords: Pregnancy · GDM · Transcriptomics · Metabonomics · Glucose · Insulin resistance

Introduction

Diabetes may be characterized as a metabolic disturbance associated with structural and functional impairment to many tissues and organs, especially the heart, blood vessels, eyes, nerves, and kidneys. The pathophysiology and etiology of hyperglycemia in pregnancy appear correlated with hormonal dyshomeostasis and may be significantly impacted by the simultaneous influence of genetic and environmental factors. Indeed, there is a gradual increase in insulin response to nutritional stimulation during pregnancy, consistent with progressive insulin resistance (1).

Gestational hyperglycemia occurs when pancreatic beta cells can no longer adequately respond to increased insulin demand during pregnancy. Gestational diabetes mellitus (GDM) is diabetes first diagnosed during pregnancy and may occur anytime during the pregnancy (most likely after 24 weeks) (2). Pregnant women who have pre-existing diabetes - type 1 diabetes, type 2 diabetes, or monogenic diabetes - may likely experience in utero hyperglycemia (3). Therefore, hyperglycemia in pregnancy (HIP) includes GDM and diabetes in pregnancy according to the International Federation of Gynecology and Obstetrics, but GDM remains the predominant cause of HIP (75–90%) (4,5).

With increasing gestational weight gain and maternal age, the incidence of GDM has increased over recent decades (6–8). The Hyperglycemia and Adverse Pregnancy Outcome Study suggests that the frequencies of GDM varied between 9.3% and 25.5% (mean 17.8%) (9), depending on the population characteristics and diagnostic criteria. With the increasing incidence of HIP, more evidence suggests that HIP has a variety of long- and short-term effects on both mothers and offspring (**Figure 1**), including preeclampsia, prelabour rupture of membranes, hyperbilirubinemia, polyhydramnios, hypocalcemia and hypomagnesemia, stillbirth, macrosomia, preterm delivery, and hypoglycemia in the newborn, and greater risk of developing respiratory distress (10–14). Long-term adverse health implications reported in the offspring of HIP mothers include overweight and subsequent obesity, cardiovascular diseases, increased incidence of neuropsychiatric and neurodevelopmental problems, and ophthalmic diseases.

Received: May 26, 2021; Accepted: June 14, 2021.

In addition, GDM is strongly linked to metabolic disorders in adult offspring, including insulin resistance, low acute insulin secretory responses, type 2 diabetes, persistently impaired glucose tolerance, and adipokine changes (15–17). Interestingly, it has been observed that these metabolic consequences are more frequent in female offspring, suggesting sex-dependent adverse effects (15,18,19). In addition, the female offspring of GDM mothers are more likely to experience GDM during pregnancy, which is regarded as a vicious circle (20). Although the prevalence of HIP is increasing, hyperglycemia-induced impairment to the offspring's cardiovascular system is unknown. Therefore, the aim of this review is to highlight and summarize the currently known molecular and metabolic mechanisms that contribute to offspring cardiovascular system dysfunction, which may provide new insights and therapeutic options for improving the long-term health of GDM women and offspring (**Figure 2**).

1. Gene expression and transcriptional production

Pancreatic β-cells help the body respond to the decline in the mother's insulin sensitivity. When blood glucose level decreases during normal physiology, the activity of glucokinase, the main glucose sensor in pancreatic β-cells, is adaptively increased, thereby enhancing insulin secretion (21,22). Meanwhile, prolactin and placental lactogen play a maladaptive part in the occurrence and development of GDM. It has been demonstrated that pregnant mice lacking prolactin receptors develop GDM (23). The lack of placental lactogen leads to β-cell proliferation, reduction of Menin (24), induction and regulation of FoxM1 (25), and activation of the paracrine/autocrine loop that increases serotonin production (26,27).

Small non-coding RNAs (ncRNAs) constitute about 60% of human genome transcripts. They can bind to the special regions of mRNAs and regulate signal pathways, embryonic development, and pathological processes of diseases through translation inhibition or messenger degradation (28–33). Based on their length and morphology, ncRNAs that are currently of interest in research include microRNAs (under 200 ribonucleotides), long non-coding RNAs (lncRNA, longer than 200 ribonucleotides), and circular RNAs (with the covalent binding between the 3' and 5' ends) (34, 35). Studies have shown that ncRNA-mediated intracellular and intercellular communication can be observed under both physiological and pathological conditions (34, 36, 37). The expression of ncRNAs is essential for the formation of pancreatic islet cells (38). Despite their physiological significance, several ncRNAs have been found to be correlated with insulin resistance and β-cell dysfunction. In particular, the abnormal regulation of ncRNAs in utero may influence the expression of target genes in offspring and cause long-term adverse events, such as obesities and cardiac diseases (39).

Additionally, Li et al. have suggested that the low expression of plasma small nucleolar RNA host gene 17 (SNHG17) may be used as a predictor in the first semester of GDM pregnancy (40). LncRNA maternally expressed gene 3 (MEG3) is abnormally upregulated in the blood, placental chorionic trophoblast cells, and umbilical vein endothelial cells of pregnant women with GDM, and it impairs the endothelial function of the fetus through the action of miR-345-3p and microRNA-370-3p targets and the AKT signaling pathway (41, 42). A follow-up of 400 women showed that plasma MEG8 levels in GDM patients are significantly elevated. In particular, researchers are able to distinguish future GDM patients from healthy pregnant women through the plasma MEG8 levels one month before GDM diagnosis (43). Moreover, Zhang et al. showed that the expression level of lncRNA metastasis associated lung adenocarcinoma transcript 1 (MALAT1) in the case group is significantly higher than that of healthy pregnant women, suggesting that MALAT1 may also be a novel biomarker (44, 45).

Not only that, in obese mice with leptin deficiency, miR-375 was absent and thus unable to maintain insulin homeostasis, and thus develop severe diabetes (46). NcRNAs also play an important role during pregnancy - studies have found that the placenta-associated microRNA is a modulator of peroxisome proliferator-activated receptor (PPAR). PPAR is a receptor involved in capacity control, lipid metabolism and inflammation, and has been shown to be associated with type 2 diabetes (47). A recent study compared the expression of miR-143 in pharmacologically treated GDM patients and normal pregnant woman in placental tissues in vivo, and found that as a protective target, miR-143 participates in the abnormal function of mitochondria in the placenta of GDM patients by regulating enzymes in glycolysis (HK-2) (48). Additionally, a 2016 study found that at 37-40 weeks of gestation, the expression of miR-98 in the placental tissue of GDM mothers was significantly increased. The same investigators used the human cell line JEG-3 to demonstrate that miR-98 regulates the glucose uptake factor Trpc3 by directly regulating Mecp2 (49). Studies have also shown that during pregnancy, the expression of miR-218 and miR-338-3p are down-regulated, while the expression of miR-144 and miR-451 is up-regulated. Specifically, under the action of estradiol and incretins, miR-338-3p regulates the proliferation of pancreatic β-cells (50). Some investigators believe that the microRNA from placenta exosomes may reflect the metabolic state of the placenta. Therefore, Nair et al. compared the microRNA differences between the chorionic villi explants in the GDM group and the control group through next-generation sequencing. Gene target and ontology analyses show differentially expressed miRNAs participating in pathways that regulate cell migration and carbohydrate metabolism (51). Since the fetus is constantly exchanging bodily fluids with the mother in utero, ncRNAs may likely be exchanged and influence the gene expression of the offspring. Based on the regulatory effect of ncRNA on the occurrence and development of GDM, as well as its presence in peripheral blood, ncRNAs may be used as biomarkers of GDM in pregnancy, and may even be utilized to predict the future metabolism of the fetus (39).

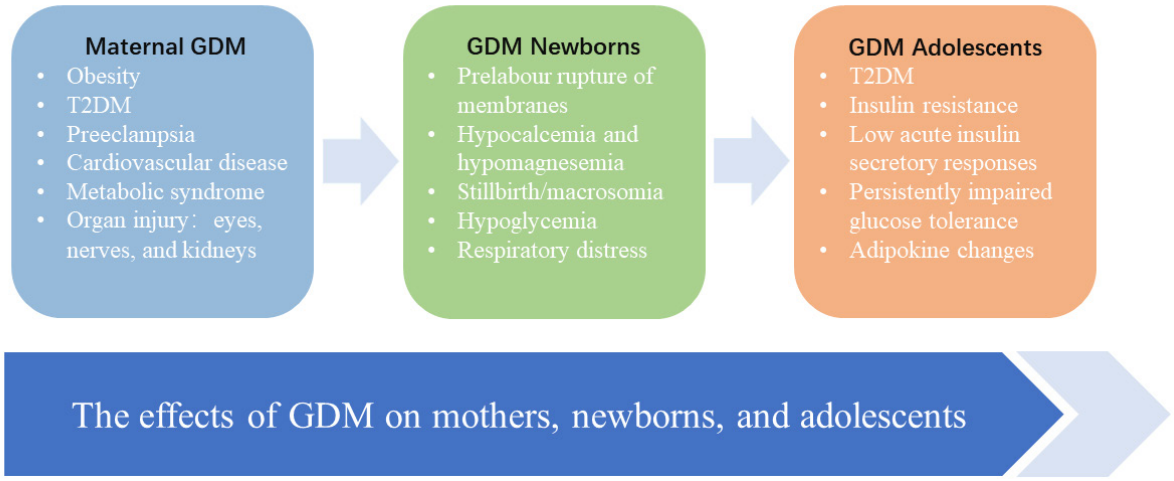

Figure 1. A variety of effects on both GDM mothers and offspring. In addition to maternal target organ damages, GDM can lead to obstetric accidents in newborns and metabolic dysfunction in adolescents. The adverse health effects of GDM in various groups are listed above.

2. Metabolomics

The high glucose environment in utero can lead to fetal metabolic disorders. This complex metabolic regulation process may partly explain the dysfunction of the cardiovascular system in the offspring. As a discipline of systematic and full-term research on low molecular weight compounds in tissues and body fluids, metabolomics can contribute to the elucidation of the mechanism of this process and reveal potential therapeutic targets and biomarkers (52). In recent years, the primary focus of metabolomics data is on the detection of pregnancy body fluid compounds of GDM mothers, including the detection of pregnant women's serum, plasma, and urine. A few other metabolomics studies collected and examined other non-traditional samples, such as fetal cord blood, urine, and meconium. Additionally, since childhood and adolescence are important periods for the development of obesity and diabetes (53, 54), there are also some metabolomics studies that examined samples from children and adolescents who have GDM mothers (55). However, despite the multitude of existing GDM metabolomics studies, a clear conclusion of metabolic profile characteristics still cannot be determined. To address this problem, future studies need to increase the number of samples in the group, compare the differences in metabolomics of samples before and after oral glucose tolerance test (OGTT), and improve the diversity of the subjects, such as their race, ethnicity, age, and living conditions.

2.1. Maternal Lipid Metabolism

A study involving 592 mothers and children tracked metabolomics data from 6-14 years old (late childhood) and 12-19 years old (adolescents) and found that female offspring that exhibited in utero hyperglycemia had increased levels of phosphatidylcholine, diacylglycerol, and phosphatidylethanolamine, which can increase the risk for obesity and higher metabolic dysfunction (56). Other studies have also shown that acetone and 3-hydroxybutyric acid are elevated in GDM, suggesting increased fatty acid catabolism (57). Indeed, another pregnancy cohort study of 178 GDM and 180 normal pregnant women showed that in addition to metabolites that participate in fatty acid oxidation, other metabolites were changed; the investigators found 17 metabolic compounds were altered (58). In the third trimester, from the control group to the mild increase in blood glucose group to the GDM group, the total fatty acids (FAs) and several specific FAs in the serum of pregnant women showed a gradually increasing trend for metabolites (59). Other studies utilizing LC-MS and GC-MS have confirmed that several lysophospholipids, taurine bile acids, and long-chain polyunsaturated fatty acid derivatives in GDM pregnant mothers are different than normal pregnancy control mothers, which may partly be responsible for changes in redox balance and low degree of inflammation (60).

2.2. Maternal Amino Acid Metabolism

Amino acids are indispensable nutrients for intrauterine growth, and the fetus carries out protein synthesis and oxidation. In addition to providing the amino acids, the placenta is also involved in protein transamination and the synthesis of some non-essential amino acids (61). Some non-essential amino acids are metabolized and delivered through interorgan cycling between the fetal liver and the placenta. The liver metabolizes glutamine (Gln) and glycine (Gly) and delivers them to the placenta as glutamate (Glu) and serine (Ser), respectively (62, 63). Therefore, the amino acid metabolism in the uterus is intimately connected to the growth of the fetus. The results of studies on mothers with type 1 diabetes show that the concentration of many amino acids increases during the first and third trimesters of pregnancy (64), which may suggest that in a state of high glucose in the uterus, the increase in amino acid metabolism and the sugar load affect fetal insulin secretion, thereby inducing

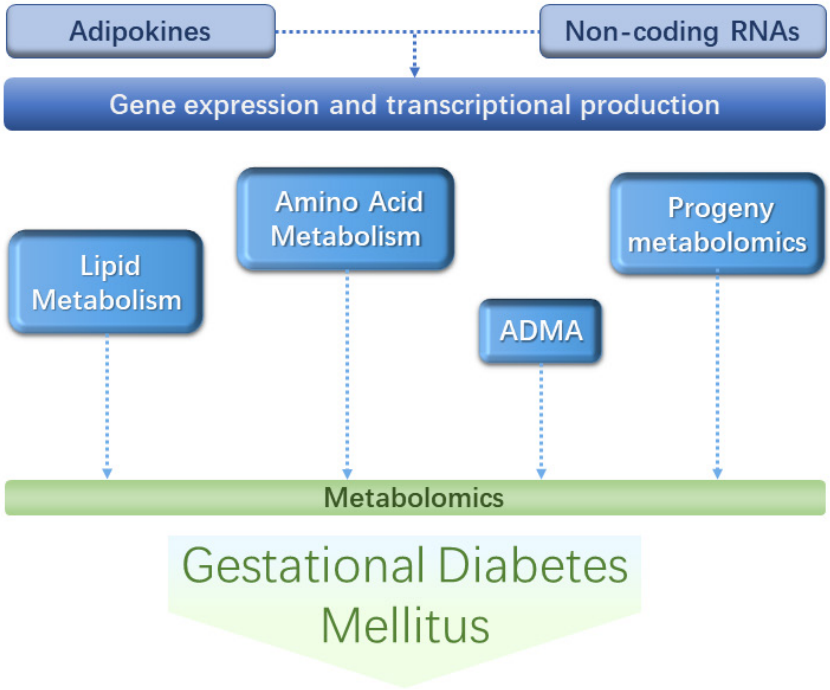

Figure 2. Conceptual diagram of associations among maternal GDM and offspring health outcomes throughout gestation to adulthood. The co-regulation of adipokines, lncRNA, and microRNA affect the metabolic changes and induce the occurrence of diseases and produce possible adverse consequences for offspring.

subsequent pathophysiological changes. Metabolomics studies of GDM mothers show that ketogenic amino acids and branched chain amino acids (BCAA) are released by skeletal muscle at a low rate and are mainly catabolized by the liver. Among them, the levels of fasting carnitine ester levels are lower, fasting β-hydroxybutyrate and free fatty acid levels are higher, and the levels of methionine, glycine, alanine, citrulline, and ornithine are significantly higher in GDM pregnant mothers relative to normal pregnant women. In normal pregnancy, proteolysis, ketogenic amino acids, and BCAA are catabolized in the liver. As a result, ketogenic amino acids are totally oxidized and gluconeogenesis is enhanced, thereby accelerating the urea cycle (65). The three common BCAA include leucine, isoleucine, and valine. In the past, researchers have found that BCAA is associated with obesity in childhood and adolescence and future insulin resistance, and studies have confirmed that nondiabetic people have lower BCAA levels compared with people who will develop type 2 diabetes later. Hence, BCAA may be a significant risk factor for diabetes (66–69). Indeed, an early study showed that the fasting and postprandial BCAA levels of the GDM population in the third trimester of pregnancy (30-39 weeks) are higher than those of the normal control pregnancy population (70). On the contrary, there are some studies showing that at 30-33 weeks and 37-41 weeks of pregnancy, there is no difference in the BCAA level in the plasma of GDM mothers relative to the normal control group. (61, 65). Some investigators believe that although BCAA may be used as a metabolic marker for predicting type 2 diabetes, it may not have the identical predictive power for GDM as anthranilic acid, alanine, glutamic acid, serine, creatinine, and allantoin; these metabolites are remarkably different between GDM pregnant population and normal pregnant population (71).

It is worth noting that in the early pregnancy metabolic map, itaconic acid, cis-aconitic acid, and acylcarnitine can be used as serum biomarkers to distinguish GDM pregnant mothers from normal pregnant women, and can be used for predicting subsequent metabolic development of GDM mothers and offspring (72, 73). Studies have demonstrated that in the first trimester of pregnancy, there are remarkable differences in the levels of arginine, glycine, and 3-hydroxyisovalerate carnitine in serum samples of GDM pregnant patients compared with serum samples of normal pregnant women (74). Results from research on GDM have demonstrated increased hypoxanthine excretion due to hypoxia and enhanced gluconeogenesis for energy supply, as well as increased production of sugar-generating amino acids and cis-aconitic acid, suggesting the need for the increase in the tricarboxylic acid cycle (57). A study that collected nuclear magnetic resonance (NMR) spectra of GDM parturients' amniotic fluid (AF) during the second trimester of pregnancy for metabolomics testing showed that abnormal fetuses seem to suffer from changes in energy metabolism and renal dysplasia. The metabolic profile of the GDM population before diagnosis indicates that as the average level of glucose increases, several amino acids, creatinine, glycerophosphocholine, acetic acid, formic acid and other compounds show a slight downward trend (73).

2.3. Maternal Asymmetric Dimethylarginine (ADMA)

Endothelial dysfunction caused by reduced bioavailability of nitric oxide (NO) is considered an early cause of atherosclerosis. Asymmetric dimethylarginine (ADMA) is an endogenous NO synthesis inhibitor, which is closely related to amino acid metabolism and participates in the metabolic process of protein modification in the cytoplasm (75). Some studies believe that it is involved in the occurrence of endothelial dysfunction and subsequent adverse cardiovascular events (76). The results of some clinical studies have shown that ADMA levels are elevated in various metabolic diseases like insulin resistance, type 2 diabetes, chronic heart failure, atherosclerosis, hypercholesterolemia, hypertension, and chronic renal failure (55). Other studies have also suggested that ADMA can be used as an independent predictor of cardiovascular death and all-cause mortality (76–79). ADMA level has been shown to exhibit a gradually increasing trend among normal pregnant mothers, impaired glucose tolerance mothers and GDM mothers, which may be significantly positively correlated with the increase in insulin and gestational age (80–82). Moreover, some studies have found that severe endothelial dysfunction exists in both IGT and GDM patients in the third trimester and is directly related to blood glucose levels. Together, these studies provide evidence that ADMA may be involved in the pathophysiological mechanism of GDM (83).

2.4. Maternal adipokines that regulate metabolism

Some adipokines play an essential role in the pathophysiological mechanism of diabetes. Studies have shown that in the second trimester of pregnancy, overweight GDM women have higher levels of leptin than normal pregnant women (21–23). At the same time, the researchers also observed that adiponectin decreases in the first 1-3 months of GDM pregnancy (24, 25). Therefore, some researchers suggest that the ratio of adiponectin to leptin (usually < 0.33, at 6-14 weeks of pregnancy) may be a predictor of GDM (26). Additionally, in the third trimester of pregnancy, cytokines such as high-sensitivity C-reactive protein (hs-CRP) and tumor necrosis factor alpha (TNF-α) in the serum of GDM women are higher than those of normal pregnant women (27–29). It has also been found that in the 24-28th week of pregnancy, the plasminogen activator inhibitor-1 (PAI-1) of GDM women is elevated significantly (29). Moreover, visfatin increases at 11-13 weeks of GDM women(30). In contrast, omentin-1 is reduced in the second trimester of GDM women (31). Studies have also reported that FABP4 is elevated in the first and third semesters (32–34), while plasma RBP4 levels are high in the first two months of GDM pregnancy (25, 35). Furthermore, in the third semester of GDM, some researchers have noted elevated levels of fibroblast growth factor-23 (FGF-23) (36).

2.5. Progeny metabolomics

In recent years, in addition to focusing on the metabolomics samples of GDM mothers, researchers have also examined the effect of GDM on the metabolomics of offspring. Studies have performed nuclear magnetic resonance spectrum analysis on the umbilical cord serum of newborns and found that the offspring samples from GDM mothers have lower glucose levels than the control group, and detected the increase of pyruvate, histidine, alanine, valine, methionine, arginine, lysine, hypoxanthine, lipoprotein and lipid levels (84). Researchers have found that 14 meconium metabolism markers and 3 urinary metabolism markers, of which four meconium metabolism biomarkers (taurodeoxycholic acid, glycocholic acid, oxytrihydroxy leukotriene B4, and DHAP (8:0) is closely involved in lipid metabolism (85). It is highly probable that the specific changes in GDM offspring after birth and even the susceptibility of diseases in adulthood may be due to alterations in lipid metabolism pathways (phospholipids, taurine-bound bile acids, and long-chain polyunsaturated fatty acid derivatives) (60).

Changes in the levels of endogenous biomarkers indicate that there is an increase in glucose, amino acids, and fatty acid assimilation in GDM, as well as the co-regulation of adipokines, lncRNA, and microRNA. The combined effect of these factors will affect fetal insulin secretion (86), which may induce the occurrence of diseases and produce possible adverse consequences for offspring by affecting lipid, amino acid, purine metabolism. Unbalanced lipid metabolism seems to be a characteristic feature of GDM.

Conflict of interest

The authors declare that there is no conflict of interests regarding the publication of this paper.

Funding

The study was supported by National Natural Science Foundation of China grants 81741050 and 8187350 (XL) and NIH F32 HL149288 Postdoctoral Research Fellowship (PNT).

References

1. Butte NF. Carbohydrate and lipid metabolism in pregnancy: normal compared with gestational diabetes mellitus. Am J Clin Nutr. 2000, 71(5 Suppl):1256S-61S.
2. Knowler WC, Barrett-Connor E, Fowler SE, Hamman RF, Lachin JM, Walker EA, et al. Reduction in the incidence of type 2 diabetes with lifestyle intervention or metformin. N Engl J Med. 2002, 346(6):393–403.
3. American Diabetes Association. 2. Classification and Diagnosis of Diabetes: Standards of Medical Care in Diabetes-2018. Diabetes Care. 2018, 41(Suppl 1):S13–27.
4. Tuomilehto J, Lindström J, Eriksson JG, Valle TT, Hämäläinen H, Ilanne-Parikka P, et al. Prevention of type 2 diabetes mellitus by changes in lifestyle among subjects with impaired glucose tolerance. N Engl J Med., 344(18):1343–50.
5. Herman WH, Hoerger TJ, Brandle M, Hicks K, Sorensen S, Zhang P, et al. The cost-effectiveness of lifestyle modification or metformin in preventing type 2 diabetes in adults with impaired glucose tolerance. Ann Intern Med. 2005,142(5):323–32.
6. Lavery JA, Friedman AM, Keyes KM, Wright JD, Ananth CV. Gestational diabetes in the United States: temporal changes in prevalence rates between 1979 and 2010. BJOG Int J Obstet Gynaecol. 2017, 124(5):804–13.
7. Goldstein RF, Abell SK, Ranasinha S, Misso M, Boyle JA, Black MH, et al. Association of gestational weight gain with maternal and infant outcomes: a systematic review and

meta-analysis. JAMA. 2017, 317(21):2207–25.
8. Hedderson MM, Williams MA, Holt VL, Weiss NS, Ferrara A. Body mass index and weight gain prior to pregnancy and risk of gestational diabetes mellitus. Am J Obstet Gynecol. 2008, 198(4):409.e1-7.
9. Sacks DA, Hadden DR, Maresh M, Deerochanawong C, Dyer AR, Metzger BE, et al. Frequency of gestational diabetes mellitus at collaborating centers based on IADPSG consensus panel–recommended criteria: the hyperglycemia and adverse pregnancy outcome (HAPO) study. Diabetes Care. 2012, 35(3):526–8.
10. Cheng YW, Block-Kurbisch I, Caughey AB. Carpenter-Coustan criteria compared with the national diabetes data group thresholds for gestational diabetes mellitus. Obstet Gynecol. 2009, 114(2 Pt 1):326–32.
11. Malcolm J. Through the looking glass: gestational diabetes as a predictor of maternal and offspring long-term health. Diabetes Metab Res Rev. 2012, 28(4):307–11.
12. Crowther CA, Hiller JE, Moss JR, McPhee AJ, Jeffries WS, Robinson JS, et al. Effect of treatment of gestational diabetes mellitus on pregnancy outcomes. N Engl J Med. 2005, 352(24):2477–86.
13. Catalano PM, McIntyre HD, Cruickshank JK, McCance DR, Dyer AR, Metzger BE, et al. The hyperglycemia and adverse pregnancy outcome study: associations of GDM and obesity with pregnancy outcomes. Diabetes Care. 2012, 35(4):780–6.
14. Michael Weindling A. Offspring of diabetic pregnancy: short-term outcomes. Semin Fetal Neonatal Med. 2009, 14(2):111–8.
15. Krishnaveni GV, Veena SR, Hill JC, Kehoe S, Karat SC, Fall CHD. Intrauterine exposure to maternal diabetes is associated with higher adiposity and insulin resistance and clustering of cardiovascular risk markers in Indian children. Diabetes Care. 2010, 33(2):402–4.
16. West NA, Crume TL, Maligie MA, Dabelea D. Cardiovascular risk factors in children exposed to maternal diabetes in utero. Diabetologia. 2011, 54(3):504–7.
17. Gautier JF, Wilson C, Weyer C, Mott D, Knowler WC, Cavaghan M, et al. Low acute insulin secretory responses in adult offspring of people with early onset type 2 diabetes. Diabetes. 2001, 50(8):1828–33.
18. Nijs H, Benhalima K. Gestational diabetes mellitus and the long-term risk for glucose intolerance and overweight in the offspring: a narrative review. J Clin Med. 2020, 22;9(2).
19. Tam WH, Ma RCW, Ozaki R, Li AM, Chan MHM, Yuen LY, et al. In utero exposure to maternal hyperglycemia increases childhood cardiometabolic risk in offspring. Diabetes Care. 2017, 40(5):679–86.
20. Lambrinoudaki I, Vlachou SA, Creatsas G. Genetics in gestational diabetes mellitus: association with incidence, severity, pregnancy outcome and response to treatment. Curr Diabetes Rev. 2010, 6(6):393–9.
21. Sorenson RL, Brelje TC. Prolactin receptors are critical to the adaptation of islets to pregnancy. Endocrinology. 2009, 150(4):1566–9.
22. Butler AE, Cao-Minh L, Galasso R, Rizza RA, Corradin A, Cobelli C, et al. Adaptive changes in pancreatic beta cell fractional area and beta cell turnover in human pregnancy. Diabetologia. 2010, 53(10):2167–76.
23. Huang C, Snider F, Cross JC. Prolactin receptor is required for normal glucose homeostasis and modulation of beta-cell mass during pregnancy. Endocrinology. 2009, 150(4):1618–26.
24. Karnik SK, Chen H, McLean GW, Heit JJ, Gu X, Zhang AY, et al. Menin controls growth of pancreatic beta-cells in pregnant mice and promotes gestational diabetes mellitus. Science. 2007, 318(5851):806–9.
25. Zhang H, Zhang J, Pope CF, Crawford LA, Vasavada RC, Jagasia SM, et al. Gestational diabetes mellitus resulting from impaired beta-cell compensation in the absence of FoxM1, a novel downstream effector of placental lactogen. Diabetes. 2010, 59(1):143–52.
26. Kim H, Toyofuku Y, Lynn FC, Chak E, Uchida T, Mizukami H, et al. Serotonin regulates pancreatic beta cell mass during pregnancy. Nat Med. 2010, 16(7):804–8.
27. Schraenen A, Lemaire K, de Faudeur G, Hendrickx N, Granvik M, Van Lommel L, et al. Placental lactogens induce serotonin biosynthesis in a subset of mouse beta cells during pregnancy. Diabetologia. 2010, 53(12):2589–99.
28. Baek D, Villén J, Shin C, Camargo FD, Gygi SP, Bartel DP. The impact of microRNAs on protein output. Nature. 2008, 455(7209):64–71.
29. Bartel DP. MicroRNAs: target recognition and regulatory functions. Cell. 2009, 136(2):215–33.
30. Mattick JS, Makunin IV. Non-coding RNA. Hum Mol Genet. 2006, 15 Spec No 1:R17-29.
31. Djebali S, Davis CA, Merkel A, Dobin A, Lassmann T, Mortazavi A, et al. Landscape of transcription in human cells. Nature. 2012, 489(7414):101–8.
32. ENCODE Project Consortium. The ENCODE (ENCyclopedia Of DNA Elements) Project. Science. 2004, 306(5696):636–40.
33. Anastasiadou E, Jacob LS, Slack FJ. Non-coding RNA networks in cancer. Nat Rev Cancer. 2018, 18(1):5–18.
34. Anfossi S, Babayan A, Pantel K, Calin GA. Clinical utility of circulating non-coding RNAs - an update. Nat Rev Clin Oncol. 2018, 15(9):541–63.
35. Chen B, Huang S. Circular RNA: An emerging non-coding RNA as a regulator and biomarker in cancer. Cancer Lett. 2018, 418:41–50.
36. Chen X, Liang H, Zhang J, Zen K, Zhang C-Y. Secreted microRNAs: a new form of intercellular communication. Trends Cell Biol. 2012, 22(3):125–32.
37. Guarino E, Delli Poggi C, Grieco GE, Cenci V, Ceccarelli E, Crisci I, et al. Circulating microRNAs as biomarkers of gestational diabetes mellitus: updates and perspectives. Int J Endocrinol. 2018;2018:6380463.
38. Lynn FC, Skewes-Cox P, Kosaka Y, McManus MT, Harfe BD, German MS. MicroRNA expression is required for pancreatic islet cell genesis in the mouse. Diabetes. 2007, 56(12):2938–45.
39. Filardi T, Catanzaro G, Mardente S, Zicari A, Santangelo C, Lenzi A, et al. Non-Coding RNA: role in gestational diabetes pathophysiology and complications. Int J Mol Sci. 2020, 21(11).
40. Li J, Du B, Geng X, Zhou L. lncRNA SNHG17 is Downregulated in Gestational Diabetes Mellitus (GDM) and Has Predictive Values. Diabetes Metab Syndr Obes Targets Ther. 2021, 14:831–8.
41. Zhang H. Mechanism associated with aberrant lncRNA MEG3 expression in gestational diabetes mellitus. Exp Ther Med. 2019, 18(5):3699–706.
42. Ye H-H, Yang S-H, Zhang Y. MEG3 damages fetal endothelial function induced by gestational diabetes mellitus via AKT pathway. Eur Rev Med Pharmacol Sci. 2018, 22(24):8553–60.
43. Zhang W, Cao D, Wang Y, Ren W. LncRNA MEG8 is upregulated in gestational diabetes mellitus (GDM) and predicted kidney injury. J Diabetes Complications. 2021 Jan;35(1):107749.
44. Zhang Y, Wu H, Wang F, Ye M, Zhu H, Bu S. Long non-coding RNA MALAT1 expression in patients with gestational diabetes mellitus. Int J Gynaecol Obstet Off Organ Int Fed Gynaecol Obstet. 2018, 140(2):164–9.
45. Zhang Y, Qu L, Ni H, Wang Y, Li L, Yang X, et al. Expression and function of lncRNA MALAT1 in gestational diabetes mellitus. Adv Clin Exp Med Off Organ Wroclaw Med Univ. 2020, 29(8):903–10.
46. Poy MN, Hausser J, Trajkovski M, Braun M, Collins S, Rorsman P, et al. miR-375 maintains normal pancreatic alpha- and beta-cell mass. Proc Natl Acad Sci U S A. 2009, 106(14):5813–8.
47. Grygiel-Górniak B. Peroxisome proliferator-activated receptors and their ligands: nutritional and clinical

implications--a review. Nutr J. 2014, 13:17.
48. Muralimanoharan S, Maloyan A, Myatt L. Mitochondrial function and glucose metabolism in the placenta with gestational diabetes mellitus: role of miR-143. Clin Sci Lond Engl 1979. 2016, 130(11):931–41.
49. Cao J-L, Zhang L, Li J, Tian S, Lv X-D, Wang X-Q, et al. Up-regulation of miR-98 and unraveling regulatory mechanisms in gestational diabetes mellitus. Sci Rep. 2016, 6:32268.
50. Jacovetti C, Abderrahmani A, Parnaud G, Jonas J-C, Peyot M-L, Cornu M, et al. MicroRNAs contribute to compensatory β cell expansion during pregnancy and obesity. J Clin Invest. 2012, 122(10):3541–51.
51. Nair S, Jayabalan N, Guanzon D, Palma C, Scholz-Romero K, Elfeky O, et al. Human placental exosomes in gestational diabetes mellitus carry a specific set of miRNAs associated with skeletal muscle insulin sensitivity. Clin Sci Lond Engl 1979. 2018, 132(22):2451–67.
52. Hivert MF, Perng W, Watkins SM, Newgard CS, Kenny LC, Kristal BS, et al. Metabolomics in the developmental origins of obesity and its cardiometabolic consequences. J Dev Orig Health Dis. 2015, 6(2):65–78.
53. Spalding KL, Arner E, Westermark PO, Bernard S, Buchholz BA, Bergmann O, et al. Dynamics of fat cell turnover in humans. Nature. 2008, 453(7196):783–7.
54. Alberga AS, Sigal RJ, Goldfield G, Prud'homme D, Kenny GP. Overweight and obese teenagers: why is adolescence a critical period? Pediatr Obes. 2012, 7(4):261–73.
55. Huynh J, Xiong G, Bentley-Lewis R. A systematic review of metabolite profiling in gestational diabetes mellitus. Diabetologia. 2014, 57(12):2453–64.
56. Perng W, Ringham BM, Smith HA, Michelotti G, Kechris KM, Dabelea D. A prospective study of associations between in utero exposure to gestational diabetes mellitus and metabolomic profiles during late childhood and adolescence. Diabetologia. 2020, 63(2):296–312.
57. Diaz SO, Pinto J, Graça G, Duarte IF, Barros AS, Galhano E, et al. Metabolic biomarkers of prenatal disorders: an exploratory NMR metabonomics study of second trimester maternal urine and blood plasma. J Proteome Res. 2011, 10(8):3732–42.
58. Enquobahrie DA, Denis M, Tadesse MG, Gelaye B, Ressom HW, Williams MA. Maternal Early Pregnancy Serum Metabolites and Risk of Gestational Diabetes Mellitus. J Clin Endocrinol Metab. 2015, 100(11):4348–56.
59. Chen X, Scholl TO, Leskiw M, Savaille J, Stein TP. Differences in maternal circulating fatty acid composition and dietary fat intake in women with gestational diabetes mellitus or mild gestational hyperglycemia. Diabetes Care. 2010, 33(9):2049–54.
60. Dudzik D, Zorawski M, Skotnicki M, Zarzycki W, Kozlowska G, Bibik-Malinowska K, et al. Metabolic fingerprint of Gestational Diabetes Mellitus. J Proteomics. 2014, 103:57–71.
61. Cetin I, de Santis MSN, Taricco E, Radaelli T, Teng C, Ronzoni S, et al. Maternal and fetal amino acid concentrations in normal pregnancies and in pregnancies with gestational diabetes mellitus. Am J Obstet Gynecol. 2005, 192(2):610–7.
62. Vaughn PR, Lobo C, Battaglia FC, Fennessey PV, Wilkening RB, Meschia G. Glutamine-glutamate exchange between placenta and fetal liver. Am J Physiol. 1995, 268(4 Pt 1):E705-711.
63. Cetin I, Fennessey PV, Quick AN, Marconi AM, Meschia G, Battaglia FC, et al. Glycine turnover and oxidation and hepatic serine synthesis from glycine in fetal lambs. Am J Physiol. 1991, 260(3 Pt 1):E371-378.
64. Kalkhoff RK, Kandaraki E, Morrow PG, Mitchell TH, Kelber S, Borkowf HI. Relationship between neonatal birth weight and maternal plasma amino acid profiles in lean and obese nondiabetic women and in type I diabetic pregnant women. Metabolism. 1988, 37(3):234–9.
65. Pappa KI, Vlachos G, Theodora M, Roubelaki M, Angelidou K, Antsaklis A. Intermediate metabolism in association with the amino acid profile during the third trimester of normal pregnancy and diet-controlled gestational diabetes. Am J Obstet Gynecol. 2007, 196(1):65.e1-5.
66. McCormack SE, Shaham O, McCarthy MA, Deik AA, Wang TJ, Gerszten RE, et al. Circulating branched-chain amino acid concentrations are associated with obesity and future insulin resistance in children and adolescents. Pediatr Obes. 2013, 8(1):52–61.
67. Friedrich N. Metabolomics in diabetes research. J Endocrinol. 2012, 215(1):29–42.
68. Roberts LD, Koulman A, Griffin JL. Towards metabolic biomarkers of insulin resistance and type 2 diabetes: progress from the metabolome. Lancet Diabetes Endocrinol. 2014, 2(1):65–75.
69. Newgard CB, An J, Bain JR, Muehlbauer MJ, Stevens RD, Lien LF, et al. A branched-chain amino acid-related metabolic signature that differentiates obese and lean humans and contributes to insulin resistance. Cell Metab. 2009, 9(4):311–26.
70. Metzger BE, Phelps RL, Freinkel N, Navickas IA. Effects of gestational diabetes on diurnal profiles of plasma glucose, lipids, and individual amino acids. Diabetes Care. 1980 , 3(3):402–9.
71. Bentley-Lewis R, Huynh J, Xiong G, Lee H, Wenger J, Clish C, et al. Metabolomic profiling in the prediction of gestational diabetes mellitus. Diabetologia. 2015, 58(6):1329–32.
72. de Seymour JV, Conlon CA, Sulek K, Villas Bôas SG, McCowan LME, Kenny LC, et al. Early pregnancy metabolite profiling discovers a potential biomarker for the subsequent development of gestational diabetes mellitus. Acta Diabetol. 2014, 51(5):887–90.
73. Graca G, Duarte IF, Barros AS, Goodfellow BJ, Diaz SO, Pinto J, et al. Impact of prenatal disorders on the metabolic profile of second trimester amniotic fluid: a nuclear magnetic resonance metabonomic study. J Proteome Res. 2010, 9(11):6016–24.
74. Nevalainen J, Sairanen M, Appelblom H, Gissler M, Timonen S, Ryynänen M. First-Trimester Maternal Serum Amino Acids and Acylcarnitines Are Significant Predictors of Gestational Diabetes. Rev Diabet Stud RDS. 2016, 13(4):236–45.
75. Mannino GC, Pezzilli S, Averta C, Fuoco A, Spiga R, Mancuso E, et al. A functional variant of the dimethylarginine dimethylaminohydrolase-2 gene is associated with myocardial infarction in type 2 diabetic patients. Cardiovasc Diabetol. 2019, 18(1):102.
76. Lu T-M, Ding Y-A, Lin S-J, Lee W-S, Tai H-C. Plasma levels of asymmetrical dimethylarginine and adverse cardiovascular events after percutaneous coronary intervention. Eur Heart J. 2003, 24(21):1912–9.
77. Valkonen VP, Päivä H, Salonen JT, Lakka TA, Lehtimäki T, Laakso J, et al. Risk of acute coronary events and serum concentration of asymmetrical dimethylarginine. Lancet Lond Engl. 2001, 358(9299):2127–8.
78. Meinitzer A, Seelhorst U, Wellnitz B, Halwachs-Baumann G, Boehm BO, Winkelmann BR, et al. Asymmetrical dimethylarginine independently predicts total and cardiovascular mortality in individuals with angiographic coronary artery disease (the Ludwigshafen Risk and Cardiovascular Health study). Clin Chem. 2007 , 53(2):273–83.
79. Böger RH. Asymmetric dimethylarginine (ADMA) and cardiovascular disease: insights from prospective clinical trials. Vasc Med Lond Engl. 2005, 10 Suppl 1:S19-25.
80. Akturk M, Altinova A, Mert I, Dincel A, Sargin A, Buyukkagnici U, et al. Asymmetric dimethylarginine concentrations are elevated in women with gestational diabetes. Endocrine. 2010, 38(1):134–41.
81. Telejko B, Zonenberg A, Kuzmicki M, Modzelewska A, Niedziolko-Bagniuk K, Ponurkiewicz A, et al. Circulating asymmetric dimethylarginine, endothelin-1 and cell adhesion molecules in women with gestational diabetes. Acta Diabetol.

2009, 46(4):303–8.
82. Sertkaya AC, Kafkasli A, Turkcuoglu I, Karabulut AB. Asymmetric dimethylarginine level in hyperglycemic gestation. Endocrine. 2011, 40(2):237–42.
83. Paradisi G, Biaggi A, Ferrazzani S, De Carolis S, Caruso A. Abnormal carbohydrate metabolism during pregnancy : association with endothelial dysfunction. Diabetes Care. 2002, 25(3):560–4.
84. Dani C, Bresci C, Berti E, Ottanelli S, Mello G, Mecacci F, et al. Metabolomic profile of term infants of gestational diabetic mothers. J Matern-Fetal Neonatal Med Off J Eur Assoc Perinat Med Fed Asia Ocean Perinat Soc Int Soc Perinat Obstet. 2014, 27(6):537–42.
85. Peng S, Zhang J, Liu L, Zhang X, Huang Q, Alamdar A, et al. Newborn meconium and urinary metabolome response to maternal gestational diabetes mellitus: a preliminary case-control study. J Proteome Res. 2015, 14(4):1799–809.
86. Mitanchez D, Yzydorczyk C, Simeoni U. What neonatal complications should the pediatrician be aware of in case of maternal gestational diabetes? World J Diabetes. 2015, 6(5):734–43.

RESEARCH ARTICLE

Multivariable analysis for complete resection rate of 10-20 mm non-metastatic rectal neuroendocrine tumors: a retrospective clinical study

Xinqiang ZHU[1, 2, #], Gang ZHOU[3, #], Linchun WEN[4], Jianing LIU[5], Xuetong JIANG[2], Jianqiang WU[2], Hailong HUANG[2], Xiaohong SHI[6], Xiaoling JIANG[6], Chungen XING[1, *]

[1] *Department of General Surgery, the Second Affiliated Hospital of Soochow University, No.1055 Sanxiang Road, Suzhou 215004, Jiangsu, China.*
[2] *Department of General Surgery, the Affiliated Suqian Hospital of Xuzhou Medical University, No.138 Huanghe South Road, Suqian 223800, Jiangsu, China.*
[3] *Department of Gastrointestinal Pancreatic Surgery, the Affiliated Jiangning Hospital of Nanjing Medical University, NO.169 Hushan Road, Nanjing 211100, Jiangsu, China.*
[4] *Department of Oncology, the Affiliated Suqian Hospital of Xuzhou Medical University, No.138 Huanghe South Road, Suqian 223800, Jiangsu, China.*
[5] *Department of Digestive, the Affiliated Suqian Hospital of Xuzhou Medical University, No.138 Huanghe South Road, Suqian 223800, Jiangsu, China.*
[6] *Department of Pathology, the Affiliated Suqian Hospital of Xuzhou Medical University, No.138 Huanghe South Road, Suqian 223800, Jiangsu, China*

 # these authors contributed equally to this work.

*Correspondence: Xingcg@suda.edu.cn
https://doi.org/10.37175/stemedicine.v2i7.89

ABSTRACT

Background: This retrospective study aimed to identify key factors affecting the rate of complete resection for non-metastatic rectal neuroendocrine tumors (NETs) using both transanal local excision (TLE) and endoscopic submucosal dissection (ESD).

Methods: Records in the past 10 years were retrieved, for a total of 95 patients diagnosed with non-metastatic rectal NETs sized between 10-20 mm. Treatment outcomes were first compared between TLE and ESD to identify significantly associated factors. Monofactor analysis was then performed between complete and local resections to identify risk factors, which were then subjected to a multivariable analysis to identify independent risk factors.

Results: Treatment outcomes between TLE and ESD were significantly associated with depth of invasion (P=0.039) and complete/local resection (P=0.048). By monofactor analysis between complete and local resections, depth of invasion, tumor size, tumor stage and endoscopic manifestation were identified to be risk factors (P=0.014, 0.003, 0.002 and 0.028, respectively). In subsequent multivariable analysis, depth of invasion and tumor size were independent risk factors, with odds ratio of 18.838 and 37.223, and 95% confidence interval of 1.242-285.800 and 2.839-488.078, respectively.

Conclusion: Depth of invasion and tumor size were independent risk factors that significantly affect the complete resection rate of 10-20 mm non-metastatic rectal NETs.

Keywords: Rectal neuroendocrine tumors · Multivariable analysis · Transanal local excision · Endoscopic submucosal dissectionscriptome · Metastasis

Introduction

Neuroendocrine tumors (NETs) is a type of gastrointestinal NETs in the rectum, which constitutes over 30% of all gastrointestinal NET diagnosis and ranks the most frequent only after small bowel NETs (1). The incidence rate of rectal NETs has risen by nearly 10 times in the past 3 decades (2). This sharp increase is thought to be a result of elevated awareness of the disease development, as well as improved preventive screening for colorectal cancer, because significant fraction of renal

Received: May 19, 2021; Accepted: June 14, 2021.

neoplasms are of low grade/stage at diagnosis (3, 4). It's estimated that at the time of diagnosis, approximately 80% of rectal NETs are less than 10 mm in diameter, with no indication of invasion or metastasis (5). According to European Neuroendocrine Tumor Society (ENETS) guidelines, medium sized rectal NETs (10-20 mm) are considered to have low risk of metastasis, for which adequate local resection is appropriate (6, 7).

Conventional polypectomy has been used to treat rectal NETs, but its efficacy is less than ideal for tumors with submucosal invasion (8, 9), therefore novel improved techniques, including endoscopic submucosal dissection (ESD) and endoscopic mucosal resection (EMR), are developed (2). EMR is advantageous over conventional polypectomy because submucosal injection produces a peduncle to lift the rectal NET away from the muscularis propria thereby enabling simple resection with snare cautery (1). Similar to EMR, tumors are also lifted out of the muscularis propria layer through submucosal injection in ESD, which has been consistently suggested to yield higher rate of complete resection than EMR (10, 11). However, compared to EMR, ESD is associated with increased incidence of complications and adverse events, including bowel perforation and delayed bleeding post-procedure (2).

In this retrospective study, we retrieved records in the past 10 years, including a total of 95 patients diagnosed with non-metastatic rectal NETs sized between 10-20 mm. Risk factors affecting the rate of complete resection for non-metastatic rectal NETs between transanal local excision (TLE) and ESD were analyzed and hereby reported.

Materials and Methods

Ethical statements

The current retrospective study was approved by the Ethical Committee of the Affiliated Suqian Hospital of Xuzhou Medical University and the Affiliated Jiangning Hospital of Nanjing Medical University. All patients provided written consent forms, and their records were used anonymously.

Inclusion and exclusion criteria

Patients with records that met these inclusion criteria were included: 1) being diagnosed of rectal NET with a size between 10-20 mm; 2) with clear endoscopic images and complete post-operation pathology and immunohistochemistry results; 3) with complete baseline characteristics including magnetic resonance imaging (MRI), computerized tomography (CT) and hematology results; 4) without local or distant metastasis; 5) received either TLE or ESD surgical treatments; 6) with tumor stage classification using post-operation tissue sample based on the 2010 World Health Organization (WHO) classification (12). Patient records were excluded if they were: 1) with non-rectal NETs or mixed adeno-neuroendocrine carcinoma; 2) with rectal NETs smaller than 10 mm or larger than 20 mm.

Patients

Records of a total of 95 patients with rectal NETs, who were admitted in the Affiliated Suqian Hospital of Xuzhou Medical University and the Affiliated Jiangning Hospital of Nanjing Medical University between January 2008 and April 2019, were eventually eligible for the current study. These 95 patients included 59 males and 36 females, aged from 29 to 58 years with a median age of 49.

Statistical analysis

SPSS 17 software was used for statistical analysis. First, chi square test was used to compare enumeration and categorical data, while Student t test was used to compare quantitative data. Significant factors were then subjected to monofactor analysis to identify risk factors differentiating between complete and local resections. Risk factors with $P < 0.05$ were further subjected to multivariate logistic regression analysis, to calculate odds ratio (OR) with 95% confidence interval (CI). $P < 0.05$ indicates statistical significance.

Results

Patient characteristics are listed in **Table 1**. In the total of 95 eligible patients analyzed in the current study, 59 were males and 36 were females, and their median age was 49 years old. By endoscopic examination of their rectal NETs, 39 patients presented as wide-base polyp and 56 as protrusive mass. Pre-operation trans-rectal ultrasound indicated that 47 cases had mucosal invasion and the other 48 cases had tumor invasion into the submucosa. Median distance of the NETs to anal verge was 6.5 cm, ranged from 3-15 cm. 51 patients underwent TLE while the other 44 were treated by ESD. Median tumor size of all patients was 11.5 cm, with the range 10-20 cm (by inclusion criteria). Based on WHO classification, 87 patients were in G1 stage, while 8 were in G2, and no G3 patient. Among all 95 patients, 75 cases continued with endoscopic follow-up, with a median follow-up length of 37.1 months, ranged from 3.5-113.0 months.

Next, treatment outcomes were first compared between TLE and ESD to identify significantly associated factors (**Table 2**). Among 51 TLE cases, 43 were complete resection (84.3%), while only 24 cases were complete resection in 44 ESD procedures (54.5%), with statistically significant difference (P=0.048). Depth of invasion was another significant factor between TLE and ESD (P=0.039).

Monofactor analysis was then performed between complete and local resections to identify risk factors (**Table 3**). Depth of invasion (P=0.014), tumor size (P=0.003), tumor stage (P=0.002) and endoscopic manifestation (P=0.028) were found to be significant risk factors distinguishing complete resection and local resection.

The abovementioned four single risk factors were then

Table 1. Clinical characteristics of patients.

Factors	Data
Gender (male/female)	59/36
Age, year [median (range)]	49 (29-58)
Endoscopic manifestation	
Sessile polyp	39
Protrusive mass	56
Depth of invasion	
Mucosa	47
Submucosa	48
Distance to anal verge, cm [median (range)]	6.5 (3-15)
Treatment	
TLE	51
ESD	44
Tumor size, mm [median (range)]	11.5 (10-20)
Tumor stage	
G1	87
G2	8
Cases of follow-up, n (%)	75 (78.94%)
Length of follow-up, months [median (range)]	37.1 (3.5-113.0)

subjected to multivariate logistic regression analysis, among which only depth of invasion and tumor size were calculated to be independent risk factors (**Table 4**). The OR for depth of invasion was 18.838 with 95% CI of 1.242-285.800, while the OR of tumor size was 37.223 with 95% CI of 2.839-488.078.

Discussion

Surgical strategy for rectal NETs

NETs are a type of well-differentiated epithelial neoplasm, with the main characteristic of predominant neuroendocrine differentiation. According to the 2010 WHO classification, NETs can be categorized into G1 (mitotic count < 2 per 10 high-power fields and/or Ki67 index < 3%) and G2 (mitotic count 2-20/10 high-power fields and/or Ki67 index 3-20%) stages.(6, 12) Due to low atypia and proliferation of tumor cells, rectal NETs generally present good prognosis with 5-year overall survival of 88.3 (13), with complete resection being the only guaranteed curative option (14). However, for most well-differentiated NETs of small size (< 10 mm), local resection is considered more appropriate because radical surgery carries a higher risk to benefit ratio. The metastatic risk of rectal NETs smaller than 10 mm, which can be completed resected, was considered to be only 3-9.8%,(9) whereas metastatic risk of rectal NETs between 10-20 mm was as high as 10-15% (15). Consistent with the above reported metastasis rates, a very recent analysis has also concluded that, there is no survival benefit to radical resection of 10-20 mm, nonmetastatic rectal NETs (16). Moreover, endoscopic/local resection was also controversial due to the lack of a consistent recognition of its efficacy (17). In comparing complete vs local resections, as well as TLE vs ESD, data in our study suggested that, although ESD is a safer surgical approach, it carries certain post-operation complications especially bleeding and perforation. Despite of these complications, the outcome of ESD is not impacted by the distance of tumor to anal verge, suggesting potential clinical benefits in cases of NETs with long distance. On the other hand, we have observed that pre-operation trans-rectal ultrasound for depth of invasion also affected the surgical outcome between complete and local resections, indicating that local resection yielded better efficacy. Therefore, local resection is the preferred surgical approach for rectal NETs between 10-20 mm, when permitted by distance of tumor to anal verge. Of note, 75 patients were re-visited endoscopic examination after surgery, putting the effective follow-up rate of our study as high as 78.94%, and no recurrence was observed.

Factors contributing to degree of resection for rectal NETs

Since surgical strategies for rectal NETs are mainly determined based on tumor size and stage, accurately assessing the size and invasion depth of the tumor by trans-rectal ultrasound is of critical importance before surgery (18). Currently there has been no clear recommendation for the best endoscopic resection strategy, but recent studies have suggested that, complete tumor resection with clear surgical margin is difficult to achieve by traditional rectal endoscopic polypectomy, especially when the tumor is sessile or arises from the deep portion of the epithelial glands penetrating the mucosa into the submucosa (19). Clinical limitations still exist even though constantly improving surgical techniques have greatly

Table 2. Treatment outcomes between TLE and ESD.

Factors	TLE (n=51)	ESD (n=44)	*P* value
Age, year [median (range)]	48 (30-58)	50 (29-57)	0.445
Gender (male/female)	19/32	40/4	0.250
Degree of resection			
Complete	43	24	0.048
Local	8	20	
Endoscopic manifestation			
Sessile polyp	19	20	0.356
Protrusive mass	31	25	
Depth of invasion			
Mucosa	35	12	0.039
Submucosa	16	32	
Distance to anal verge, cm [median (range)]	6.7 (3-9)	10.1 (8-15)	0.128
Tumor size, mm [median (range)]	15.6 (10-20)	11.9 (10-19)	0.582
Tumor stage			
G1	47	40	0.963
G2	4	4	
Post-operation complications			
Bledding	8	4	0.996
Perforation	0	4	

TLE: transanal local excision; ESD: endoscopic submucosal dissection.

Table 2. Treatment outcomes between TLE and ESD.

Factors	Complete (n=67)	Local (n=28)	*P* value
Treatment			
TLE	43	8	0.112
ESD	24	20	
Gender (male/female)	31/36	28/0	0.999
Age, year [median (range)]	49 (29-58)	50 (36-57)	0.919
Depth of invasion			
Mucosa	47	0	0.014
Submucosa	20	28	
Distance to anal verge, cm [median (range)]	9 (3-15)	7 (5-10)	0.471
Tumor size, mm [median (range)]	13 (10-19)	19 (12-20)	0.003
Tumor stage			
G1	59	28	0.002
G2	8	0	
Endoscopic manifestation			
Wide-base polyp	35	4	0.028
Protrusive mass	32	24	
Post-operation complications			
Bleeding	8	4	
Perforation	0	4	0.866
None	59	20	

TLE: transanal local excision; ESD: endoscopic submucosal dissection.

Table 4. Multivariable analysis.

	B	SE	Wald	DF	Sig.	OR	95% CI of OR
Depth of invasion	2.936	1.387	4.477	1	0.034	18.838	1.242-285.800
Tumor size	3.617	1.313	7.588	1	0.006	37.223	2.839-488.078

B: B coefficient; SE: standard error; Wald: Wald chi-square test; DF: degrees of freedom; OR: odds ratio; CI: confidence interval.

increased the complete resection rate by EMR and ESD. In our present study, complete resection rate was 84.3% (43/51) for TLE and 54.5% (24/44) for ESD, respectively, and is significantly correlated with tumor size and invasion depth. Nevertheless, full-thickness excision is still a first surgical option for complete removal of rectal NETs (20, 21). in which the broadened operative field by carbon dioxide insufflations allows accurate determination of margins and the possibility of suturing. In addition, full-thickness excision greatly reduces complications such as bleeding and perforation, the latter of which could be repaired without conversion to a transabdominal approach. The 8 cases of bleeding after TLE healed spontaneously without perforation following conservative treatment. On the contrary, 4 cases of perforation occurred during ESD as a result of an effort to preserve intact samples, all of which were repaired immediately during surgery. In the actual surgeries reported here, distance of tumor to anal verge also hindered operation and consequently impacted complete resection rate, although no statistically significant correlation was observed, likely due to small sample size.

Moreover, besides tumor size (no less than 10 mm), lymphovascular invasion, muscularis invasion and mitotic count, all of which were correlated with recurrence and metastasis of rectal NETs (22, 23), histologically complete resection is also key factor in preventing recurrence and metastasis. In line with this, for rectal NETs between 10-20 mm, National Comprehensive Cancer Network has recommended rectal endoscopic follow-up at 6 and 12 months after surgery (24).

Lymph node dissection for rectal NETs

According to the European Neuroendocrine Tumor Society Consensus Guidelines, rectal NETs are considered to be indolent, and complications are only observed in a small proportion of patients. However, recent study has pointed out that, despite a relatively indolent behavior, approximately 5% of rectal NETs smaller than 10 mm are indeed malignant and can metastasize locally (25).

A retrospective study in epidemiology has found that, rectal tumors 11-19 mm in size are more frequent of lymph node involvement than smaller ones (26). Patients receiving radical excision general have higher tumor stage and/or grade, and their tumors may have invaded into the muscularis propria, which is independently correlated with lymphatic metastasis (15). Although the 5-year overall survival rate of rectal NETs is close to 85%, that with local metastasis is sharply reduced to 50%, which is further decreased merely 20% in cases with distant metastasis (27). In the present study, no lymph node involvement was detected in either TLE or ESD. Based on pre-operation trans-rectal ultrasound scan, tumor invasion was restricted to mucosa and submucosa. Therefore, even in the case of incomplete resection, a localized colectomy is still appropriate for rectal NETs smaller than 20 mm with submucosal invasion (28).

Conclusion

Both TLE and ESD are appropriate therapies to treat rectal NETs between 10-20 mm. Tumor size and invasion depth are independent risk factors associated with rate of complete resection. Cautions should be taken when treating these tumors with malignant potential in clinic, and it is critical to follow systematic diagnosis and management in latest guidelines,(29) in order to choose the therapy with the highest benefit-to-risk ratio for patients.

Conflict of interest

The authors declare that they have no conflicts of interest to disclose.

References

1 Basuroy R, Haji A, Ramage JK, Quaglia A, Srirajaskanthan R. Review article: the investigation and management of rectal neuroendocrine tumours. Aliment Pharmacol Ther. 2016;44:332-345.

2 Chablaney S, Zator ZA, Kumta NA. Diagnosis and management of rectal neuroendocrine tumors. Clin Endosc. 2017;50:530-536.

3 Dasari A, Shen C, Halperin D, Zhao B, Zhou S, Xu Y, et al. Trends in the incidence, prevalence, and survival outcomes in patients with neuroendocrine tumors in the United States. JAMA Oncol. 2017;3:1335-1342.

4 Rindi G, Petrone G, Inzani F. The 2010 WHO classification of digestive neuroendocrine neoplasms: a critical appraisal four years after its introduction. Endocr Pathol. 2014;25:186-192.

5 Davies L, Weickert MO. Gastroenteropancreatic neuroendocrine tumours: an overview. Br J Nurs. 2016;25:S12-15.

6 Caplin M, Sundin A, Nillson O, Baum RP, Klose KJ, Kelestimur F, et al. ENETS Consensus Guidelines for the management of patients with digestive neuroendocrine neoplasms: colorectal neuroendocrine neoplasms. Neuroendocrinology. 2012;95:88-97.

7 O'Toole D, Kianmanesh R, Caplin M. ENETS 2016 Consensus guidelines for the management of patients with digestive neuroendocrine tumors: an update. Neuroendocrinology. 2016;103:117-118.

8 Son HJ, Sohn DK, Hong CW, Han KS, Kim BC, Park JW, et al. Factors associated with complete local excision of small rectal carcinoid tumor. Int J Colorectal Dis. 2013;28:57-61.

9 Onozato Y, Kakizaki S, Iizuka H, Sohara N, Mori M, Itoh H.

Endoscopic treatment of rectal carcinoid tumors. Dis Colon Rectum. 2010;53:169-176.
10 He L, Deng T, Luo H. Efficacy and safety of endoscopic resection therapies for rectal carcinoid tumors: a meta-analysis. Yonsei Med J. 2015;56:72-81.
11 Zheng H, Li Y, Zhang W, Zeng F, Zhou SY, Zheng HB, et al. Electroacupuncture for patients with diarrhea-predominant irritable bowel syndrome or functional diarrhea: a randomized controlled trial. Medicine (Baltimore). 2016;95:e3884.
12 Bosman FT, Carneiro F, Hruban RH, Theise ND. WHO classification of tumours of the digestive system. Geneva: World Health Organization; 2010. 417 pp. p.
13 Modlin IM, Lye KD, Kidd M. A 5-decade analysis of 13,715 carcinoid tumors. Cancer. 2003;97:934-959.
14 Ishikawa K, Arita T, Shimoda K, Hagino Y, Shiraishi N, Kitano S. Usefulness of transanal endoscopic surgery for carcinoid tumor in the upper and middle rectum. Surg Endosc. 2005;19:1151-1154.
15 Shields CJ, Tiret E, Winter DC, International Rectal Carcinoid Study G. Carcinoid tumors of the rectum: a multi-institutional international collaboration. Ann Surg. 2010;252:750-755.
16 Fields AC, Saadat LV, Scully RE, Davids JS, Goldberg JE, Bleday R, et al. Local excision versus radical resection for 1- to 2-cm neuroendocrine tumors of the rectum: a national cancer database analysis. Dis Colon Rectum. 2019;62:417-421.
17 Moon CM, Huh KC, Jung SA, Park DI, Kim WH, Jung HM, et al. Long-term clinical outcomes of rectal neuroendocrine tumors according to the pathologic status after initial endoscopic resection: a KASID multicenter study. Am J Gastroenterol. 2016;111:1276-1285.
18 Rodrigues A, Castro-Pocas F, Pedroto I. Neuroendocrine rectal tumors: main features and management. GE Port J Gastroenterol. 2015;22:213-220.
19 Chen WJ, Wu N, Zhou JL, Lin GL, Qiu HZ. Full-thickness excision using transanal endoscopic microsurgery for treatment of rectal neuroendocrine tumors. World J Gastroenterol. 2015;21:9142-9149.
20 Kumar AS, Coralic J, Kelleher DC, Sidani S, Kolli K, Smith LE. Complications of transanal endoscopic microsurgery are rare and minor: a single institution's analysis and comparison to existing data. Dis Colon Rectum. 2013;56:295-300.
21 Flexer SM, Durham-Hall AC, Steward MA, Robinson JM. TEMS: results of a specialist centre. Surg Endosc. 2014;28:1874-1878.
22 Jernman J, Valimaki MJ, Louhimo J, Haglund C, Arola J. The novel WHO 2010 classification for gastrointestinal neuroendocrine tumours correlates well with the metastatic potential of rectal neuroendocrine tumours. Neuroendocrinology. 2012;95:317-324.
23 Konishi T, Watanabe T, Nagawa H, Oya M, Ueno M, Kuroyanagi H, et al. Treatment of colorectal carcinoids: A new paradigm. World J Gastroenterol. 2010;2:153-156.
24 Kulke MH, Shah MH, Benson AB, 3rd, Bergsland E, Berlin JD, Blaszkowsky LS, et al. Neuroendocrine tumors, version 1.2015. J Natl Compr Canc Netw. 2015;13:78-108.
25 Kasuga A, Chino A, Uragami N, Kishihara T, Igarashi M, Fujita R, et al. Treatment strategy for rectal carcinoids: a clinicopathological analysis of 229 cases at a single cancer institution. J Gastroenterol Hepatol. 2012;27:1801-1807.
26 McConnell YJ. Surgical management of rectal carcinoids: trends and outcomes from the surveillance, epidemiology, and end results database (1988 to 2012). Am J Surg. 2016;211:877-885.
27 Weinstock B, Ward SC, Harpaz N, Warner RR, Itzkowitz S, Kim MK. Clinical and prognostic features of rectal neuroendocrine tumors. Neuroendocrinology. 2013;98:180-187.
28 Ramage JK, De Herder WW, Delle Fave G, Ferolla P, Ferone D, Ito T, et al. ENETS consensus guidelines update for colorectal neuroendocrine neoplasms. Neuroendocrinology. 2016;103:139-143.
29 Kulke MH, Benson AB, 3rd, Bergsland E, Berlin JD, Blaszkowsky LS, Choti MA, et al. Neuroendocrine tumors. J Natl Compr Canc Netw. 2012;10:724-764.

RESEARCH ARTICLE

Alcoholism via 6-layer customized deep convolution neural network

Ziquan ZHU

Department of Civil Engineering, University of Florida, Gainesville, United States

*Correspondence: Zhu.ziquan@ufl.edu
https://doi.org/10.37175/stemedicine.v2i7.93

ABSTRACT

Background: Alcoholism is caused by excessive alcohol into the human body. Alcohol primarily damages the central nervous system of the human body and causes the nervous system function disorder and inhibition. Severe addiction can lead to respiratory circulation center inhibition, paralysis and even death. So far, the diagnosis of alcoholism is done by radiologist's manual CT examination. However, the diagnosis process is time-consuming, subjective and boring for doctors. External factors, such as extreme fatigue, lack of sleep and mental concentration, can easily affect the diagnosis process.

Methods: In order to solve this problem, this paper proposed a new neural network based on computer vision, which used deep convolution neural network to diagnose alcoholism automatically. A total of 216 brain images were collected. In the 6-layer customized deep convolution neural network structure, there were four convolution layers and two fully connected layers, and each convolution layer was connected with a pooling layer.

Results: The results showed that the accuracy, sensitivity, specificity, precision, F1, MCC and FMI were 95.96% ± 1.44%, 95.96% ± 1.66%, 95.95% ± 1.67%, 95.73% ± 1.72%, 95.84% ± 1.48%, 91.92% ± 2.87% and 95.84% ± 1.48% respectively.

Conclusion: It can be concluded from comparison results that the proposed neural network structure is more effective than four state-of-the-art approaches. The proposed method has high accuracy and can be used as a diagnostic method for alcoholism.

Keywords: Deep convolution neural network · CT image · Alcoholism

Introduction

Alcohol has inhibitory effect on the central nervous system, so moderate drinking will make the human body relaxed and warm, which can relieve fatigue, calm the nerves, relieve pain and help sleep. But a lot of drinking can cause harm to human body, even lead to alcoholism which refers to the mental and physical disorders caused by excessive drinking. Alcoholism can be divided into acute alcoholism and chronic alcoholism. Acute alcoholism can be caused by a large amount of drinking. A large amount of alcohol into the body would firstly cause the central nervous system excited, and then inhibit the state. In the whole process, people could do a lot of unreasonable behavior, such as giggling, crying, attacking, forgetfulness. Severe alcoholism may result in liver glucose failure, hypoglycemia, respiratory failure, circulatory failure, and even death. Long-term heavy drinking can cause chronic alcoholism, which can cause mental and physical disorders. Patients with chronic alcoholism usually have a drinking history of more than 10 years. The cerebral cortex, cerebellum, pontine and other lesions occur in the victims. In addition, the liver, heart and endocrine glands are damaged, leading to deficiency of various enzymes and vitamins in the body and severe malnutrition. Patients with this disease can develop alcohol dependence syndrome and have

Received: May 27, 2021; Accepted: June 12, 2021.

withdrawal reactions. Alcoholism, whether acute or chronic, can lead to many serious complications, and the prognosis is not optimistic.

With constant development of computer technology, computer-based technology has been applied to many fields, such as medicine. Kumar, S. et al. used support vector machine and fuzzy c-means clustering algorithm to reduce the feature dimensions of EEG, so as to detect the effect of alcohol on cerebral cortex more accurately (1). Rodrigues, J. d. C. et al. presented the classification of alcoholic electroencephalographic (EEG) signals using Wavelet Packet Decomposition (WPD) and machine learning techniques (2). Anuragi, A. et al. proposed a novel empirical wavelet transform (EWT) based machine learning framework for the classification of alcoholic and normal subjects using EEG signals (3). In the framework, the adaptive filtering is used to extract Time–Frequency-domain features from Hilbert-Huang Transform (HHT). Hou, X.-X. proposed to use Hu moment invariants (HMIs) (4). Han, L. employed three-segment encoded Jaya (3SEJ) algorithm for alcoholism recognition (5). Qian, P. presented a novel method based on cat swarm optimization (CSO) (6). Chen, X. used linear regression classifier for alcoholism detection (7).

The diagnosis of alcoholism relies on doctors' manual observation based on brain images. However, the diagnosis process is time-consuming, subjective and boring for doctors. External factors, such as extreme fatigue, lack of sleep and mental concentration, can easily affect the diagnosis process. In order to solve this problem, this paper proposed a 6-layer customized deep convolution neural network structure for automatic diagnosis of alcoholism. The main innovation and contribution of this paper: (i) we proposed an automatic diagnosis method of alcoholism based on deep convolution neural network; (ii) compared with four state-of-the-art approaches, the proposed neural network structure is more effective. Based on its excellent experimental and comparison results, the proposed neural network structure in this paper can be used as one of the methods for diagnosing alcoholism.

The rest of the structure of this paper is as follows. The second section introduces the data sources and preprocessing. The third section contains the 6-layer customized deep convolution neural network structure. The fourth section introduces the experimental results and comparison results with four state-of-the-art approaches. Section 5 discusses the conclusion, the shortcomings of this paper and the future research.

Materials

Database

In this study, only the samples that meet the standards would be used in database for further experiments. The applicants joined this research through advertisement or participated in Nanjing Brain Hospital of Jiangsu Province, Provincial Hospital and Nanjing Children's hospital. To ensure precision of the experiment, the applicants would be carefully examined and excluded those with major mental illness. Applicants that were not proficient in Putonghua would be excluded, and the data would also be rejected if applicants had the following diseases or symptoms, such as stroke, epilepsy, liver cirrhosis, liver failure and HIV. If applicants had experienced a loss of consciousness for more than 15 minutes due to seizures, we would also exclude these applicants.

With the full acknowledge and consent from the participants, it took us three years to complete the data collection. Total of 235 participants (males-117, females-118) were tested, consisted of 114 long-term abstinence participants (males-58, females-56) and 121 non-alcohol control participants (males-59, females-62). All participants were tested by the "Alcohol Use Disorder Identification Test (AUDIT)" (8). The test results are shown in **Table 1**, in grams (9).

MRI Scan

In the paper, Siemens Verio Tim 3.0T MRI scanner was used, and a total of 216 sagittal slices covering the whole brain were obtained. During the scan, all applicants remained awake, laid down quietly and closed their eyes. MP-RAGE sequence was used in 216 images covering the whole brain. In the experiment, our final image was 8-bit gray depth instead of 16 bit gray depth, because alcoholism can change brain structure, but not the gray

Table 1. Demographic characteristics.

	Alcoholic		Nonalcoholic	
	Males	Females	Males	Females
Age(y)	56.5 + 8.9	59.0 + 8.0	55.3 + 7.9	56.9+8.4
Education(y)	9.3 + 1.6	9.9 + 1.9	9.3 + 2.5	9.6+2.4
DDE(grams/d)	300.7 + 92.1	197.6 + 62.1	4.9 + 3.8	6.8+4.7
DHD(y)	19.6 + 5.4	13.2 + 3.5	0 ± 0	0±0
LOS(y)	6.7 + 3.4	9.8 + 5.1	-	-
AUDIT	25.4 + 4.9	25.1 + 4.2	1.6 + 2.2	1.5+2.0

DDE, daily drinks of ethanol; DHD, duration of heavy drinking; LOS, length of sobriety; AUDIT, alcohol use disorders identification test.

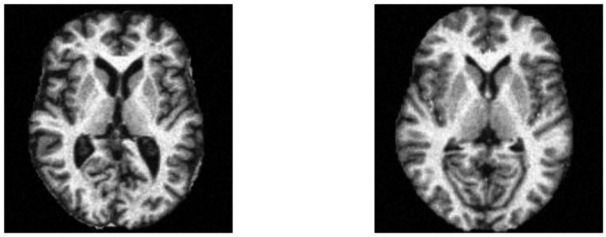

Figure 1. Slice examples.

scale of the image and another reason was that 8-bit gray depth is enough for us to complete our study. Here are our image parameters: gray level depth = 8-bit, TI = 900 ms, TR = 2000 ms, TE = 2.50 ms, FA = 9°, matrix = 256 × 256, FOV = 256 mm × 2 56 mm.

Slice

We extracted the brain from all the 3D images and removed the skull by using FSL (FMRIB Software library) (10, 11). All images were converted to MINI as standard template and sampled as 2 mm isotropic voxel, as shown in **Figure 1**. We selected the 80th slice (Z = 80.8 mm) at the coordinates of mini 152. Compared with other brain slices, this brain slice contained two characteristics of alcoholism patients: (1) small gray matter, (2) large ventricle. After clipping the background, a 176 × 176 matrix was left for subsequent training.

Methodology

The main method used in this paper is deep convolution neural network. Deep convolution neural network (DCNN) has advanced dramatically over the past decade in numerous fields related to pattern recognition from image processing to voice recognition (12). DCNN can reduce the number of parameters in neural network where this advantage makes it widely used in image recognition, speech recognition and many other fields.

Although there are many different DCNN frameworks, the basic components of DCNN framework are the same or similar, as shown in **Figure 2**. The input layer, convolution layers, pooling layers, activation layers, fully-connected layers and the output layer constitute a DCNN framework.

Convolution

The convolution layer is composed of input, convolution kernel and output. The convolution kernel is used to learn and extract input features (13, 14). In the neural network, there would be many convolution layers to increase efficiency (15). Convolution is a fairly simple operation: we start with a small weight matrix (16), the convolution kernel and let it gradually "scan" the input data. As the convolution kernel "slides", it computes the product of the weight matrix and the scanned data matrix (17), and then aggregates the results into an output pixel, the formula is as follow:

$$W\_(i+1)=(W\_i-F\_w+2P)/S+1 \quad [1]$$

$$H\_(i+1)=(H\_i-F\_h+2P)/S+1 \quad [2]$$

$$D\_(i+1)=K \quad [3]$$

In the above formula, the size of the input matrix is Wi×Hi×Di (W is width, H is height and D is depth), the size of the output matrix is $W_{i+1} \times H_{i+1} \times D_{i+1}$, F_w represents the width of the convolution kernel (18), F_h is the height of convolution kernel, P represents padding, S represents the stride, K represents the number of filters.

As shown in **Figure 3**, the input size is the matrix with the size of 4 × 4, the filter is 3 × 3 matrix and the output is the matrix with the size of 2 × 2. The filter elements at each position are multiplied by the corresponding input elements and then summed (sometimes called multiplication, summation, and addition). The results are then saved to the appropriate location in the output. The output of the convolution operation can be obtained by performing the procedure at all locations. Each step is calculated as follows:

Output1, 1=1×2+2×0+3×1+0×0+1×1+2×2+3×1+0×0+1×2=15;

Output1, 2= 2×2+3×0+0×1+1×0+2×1+3×2+0×1+1×0+2×2=16;

Output2, 1=0×2+1×0+2×1+3×0+0×1+1×2+2×1+3×0+0×2=6;

Output2, 2=1×2+2×0+3×1+0×0+1×1+2×2+3×1+0×0+1×2=15.

Pooling

Pooling is another important concept in deep convolution neural network, which is actually a form of downsampling (19). There are many different forms of nonlinear pooling functions, which "Max pooling" is the most common, as shown Figure 4. It divides the input image into several rectangular regions and outputs the maximum value for each sub region. The max pooling formula is as follows:

$$MP = \max(N_R) \quad [4]$$

In the above formula, MP is the max pooling, N represents the pooling region, R is the activation set and within the pooling region (20, 21).

Intuitively, the reason why max pooling can work effectively is that after a feature is found, its precise

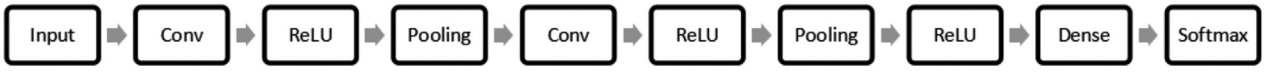

Figure 2. DCNN model.

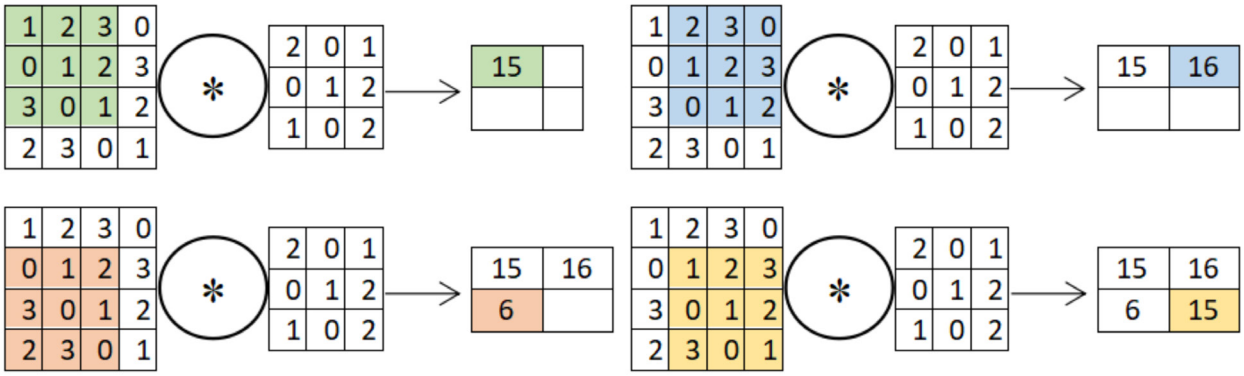

Figure 3. Convolution operation.

position is far less important than its relative position with other features [22]. The pooling layer will continuously reduce the spatial size of the data, so the number of parameters and the amount of calculation will also decrease, which also controls the over fitting to a certain extent [23, 24].

Another method is called average pooling, which is to calculate the average value of an region instead of the maximum value, as shown in Figure 4. The average pool formula is as follows:

$$AP = (\sum N_R)/|N_R| \quad [5]$$

After the pooling operation, the output size formula is as follows:

$$W_{output} = (W_{input} - G_{pooling})/S+1 \quad [6]$$

$$H_{output} = (H_{input} - G_{pooling})/S+1 \quad [7]$$

$$D_{output} = D_{input} \quad [8]$$

In the above formula, the size of the input matrix is $W_{input} \times H_{input} \times D_{input}$ (W is width, H is height and D is depth), the size of the output matrix is $W_{output} \times H_{output} \times D_{output}$, Gpooling represents the size of the pooling kernel and S represents the stride (25).

Generally speaking, the pooling layer is periodically inserted between the convolution layers of DCNN. In short, the pooling layer is to remove redundant information and retain key information.

Batch Normalization

To comprehensively study the effects of OA treatment on LPS-treated Raw264.7 cells, transcriptome analysis was conducted for the Control group, the LPS (LPS treatment alone) group, and the LPS/OA (LPS plus OA treatment) group. **Figure 4** showed the general correlation and component analysis results. As could be seen, gene profiles with changed expression levels were quite different among the three groups. However, the pattern change of the LPS group was the most significant (with a correlation of 0.92), while the correlation increased to 0.94 between the LPS/OA group and either the LPS or the Control group, suggesting that OA treatment restored, at least, part of the gene expression profiles from the LPS group to the Control group.

Batch normalization (BN) is a way to unify the scattered data and optimize the neural network. In the process of neural network training, with the increase of the network depth (26), the input value of each layer (i.e. x = Wu + B, u is the input) gradually shifts and changes (27). The reason why the training convergence is slow is that the whole distribution is close to the upper and lower limits of the value range of nonlinear function (28). Therefore, it will lead to the disappearance of the gradient of the lower layer network in the back propagation, which is the reason for training deep convolution neural network. BN is the standard normal distribution that reverses the input value of any neuron in each layer back and forth with the mean value of 0 and the variance of 1 (29).

For the deep convolution neural network, the activation value of each hidden layer of neurons can be batch standardized, which can be imagined as adding a BN operation layer to each hidden layer (30). The operation layer is located after the activation value of x = Wu + B is obtained and before the nonlinear function transformation. The specific formula of batch normalization is as follows:

$$\overline{x^{(k)}} = \frac{x^{(k)} - E[x^{(k)}]}{\sqrt{Var[x^{(k)}]}} \quad [9]$$

The $x^{(k)}$ of this layer of neurons does not refer to the original input, it is not the output of the upper layer of neurons (31), but the linear activation of this layer of neurons x = Wu + B, where u is the output of the upper layer of neurons. $E[x^{(k)}]$ is the mean and $Var[x^{(k)}]$ is the variance.

In a word, BN gradually maps the input distribution to a nonlinear function, approximates the limit saturated area of the value range, and compulsorily returns the normal distribution with the mean value of 0 and the variance of 1 (32). In this way, the input value of the nonlinear transformation function falls into the input sensitive region to avoid the problem of gradient disappearance. When the gradient is large, the efficiency of parameter adjustment can be improved and the convergence speed can be accelerated (33).

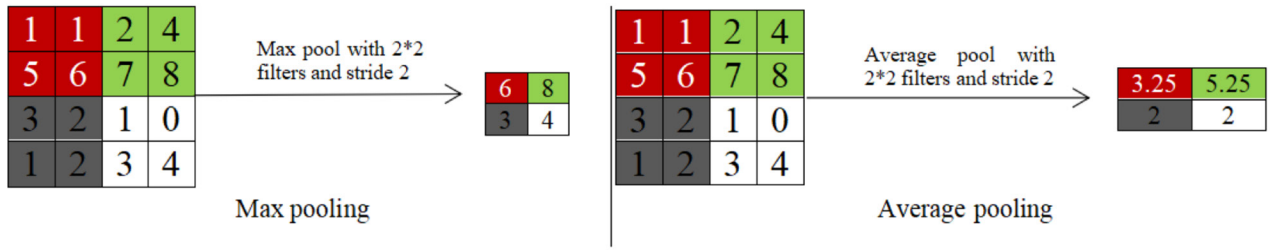

Figure 4. Pooling layer.

Rectified Linear Unit

In the neural network, the activation function is responsible for transforming the sum weighted input from the node into the activation of the node or output of the input. In order to train a deep convolution neural network with random gradient descent with error back propagation, an activation function is needed. The activation function is actually a nonlinear function that allows learning the complex relationships in the data. At the same time, it must provide higher sensitivity to activation and input and avoid easy saturation. In this paper, we used the rectified linear unit activation function (ReLu). The rectified linear unit activation function is a simple calculation, the formula is as follows:

$$\max(0, x) = \begin{cases} 0, \text{if } x \leq 0 \\ x, \text{if } x > 0 \end{cases} \quad [10]$$

The function is linear for values greater than zero. ReLu has many required properties of linear activation function. However, it is a nonlinear function because negative values always output zero. If the input is 0 or less, it returns 0. as shown in **Figure 5**.

Compared with other activation functions, such as sigmoid and tanh, ReLu is simple to calculate, because it is just a max function. ReLu can output true zero value, while sigmoid, tanh and other functions can only output very close to zero value.

Structure of customized DCNN

In this paper, we mainly used DCNN as the main method. In the DCNN structure, we used four convolution layers, four pooling layers and two fully connected layers. The number of filters in the first convolution layer was 32, the number of filters in the second and third convolution layers was 64, and the number of filters in the fourth convolution layer was 128. The filters of the four convolution layers were all matrices of 3 × 3 size. The pooling layer was connected behind each convolution layer, and the size of the four-layer pooling layer filter was 2 × 2 matrix. After convolution and pooling operation, two fully connected layers were connected. The structure and detailed parameters of DCNN are shown in **Table 2**. The specific flow chart is as shown in **Figure 6**.

After four convolution layers and four pooling layers, the output size was 11x11x128. In the first fully connected layer, the parameter value was obtained by multiplying the dense size and the processed data value. The specific calculation was 15488 × 1000 = 15488000. The calculation of the second layer was the same as that of the first fully connected layer, the parameters of the second fully connected layer were 2000 (2 × 1000 = 2000).

Measures

There will still be some deviation between the machine prediction and the actual one, so we introduce the following concepts to evaluate the performance of the classifier, such as sensitivity, specificity, and so on. Before introducing the concepts, we firstly introduce the confusion matrix. We use a two-class model, so we mix all the results of the forecast and the actual situation, as shown in **Table 3**.

Table 2. Structure of customized DCNN.

Layer	Size	Parameters
Input	176 × 176	
Conv Layer 1	88 × 88 × 32	32 3 × 3, pooling size = 2
Conv Layer 2	44 × 44 × 64	64 3 × 3, pooling size = 2
Conv Layer 3	22 × 22 × 64	64 3 × 3, pooling size = 2
Conv Layer 4	11 × 11 × 128	128 3 × 3, pooling size = 2
FCL	1000	15488 × 1000
FCL	2	2 × 1000

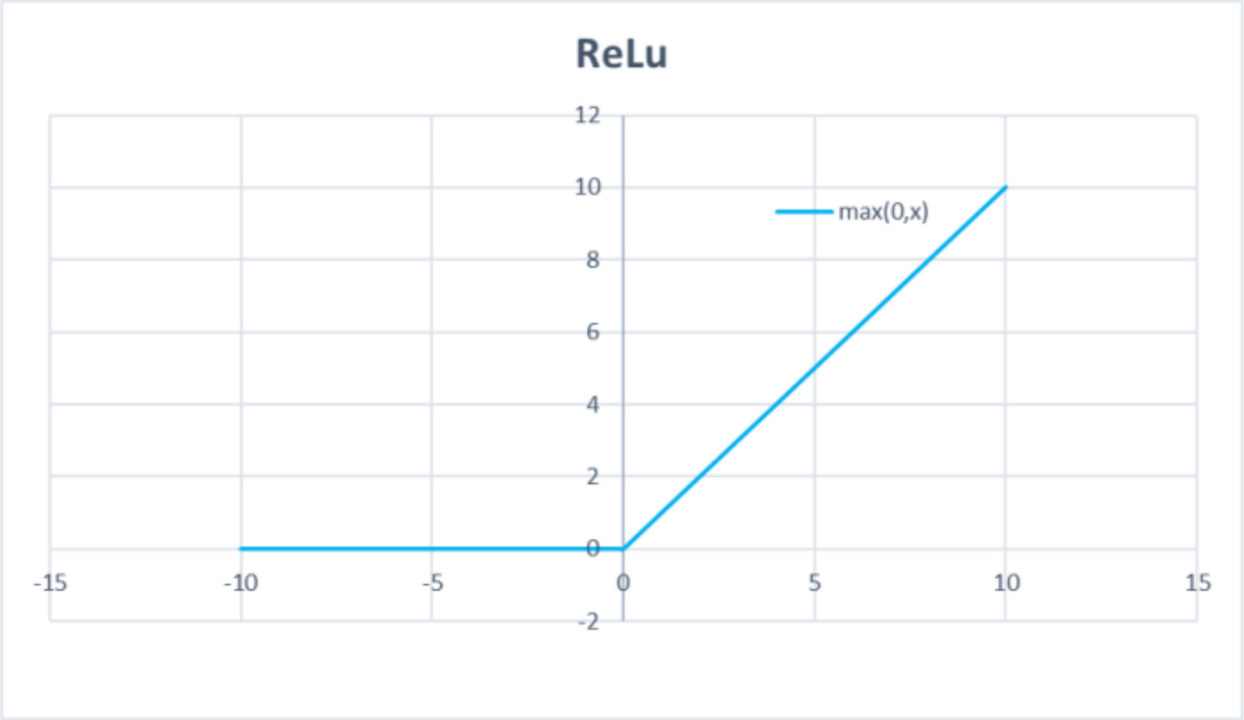

Figure 5. ReLu function.

As a result, the following four situations would appear. True positive (TP), which is called true positive rate, indicates the number of positive samples predicted by positive samples. False positive (FP), which is called false positive rate, indicates that it is the number of negative samples predicted to be positive samples. False negative (FN), which is called false negative rate, indicates that it is the number of positive samples predicted to be negative samples. True negative (TN), which is called true negative rate, indicates the number of negative samples predicted by negative samples.

Sensitivity represents the proportion of pairs in all positive cases, and measures the recognition ability of classifier to positive cases, the formula is as follows:

$$\text{Sensitivity} = TP/(TP + FN) \quad [11]$$

Specificity refers to the proportion of negative cases to all negative cases, which measures the ability of the classifier to recognize negative cases, the formula is as follows:

$$\text{Specificity} = TN/(FP + TN) \quad [12]$$

Precision is for the prediction results. It means the probability of the actual positive samples among all the predicted positive samples. It means how many of the predicted positive samples can we predict correctly, the formula is as follows:

$$\text{Precision} = TP/(TP + FP) \quad [13]$$

Accuracy is defined as the percentage of the total sample that predicted the correct results, the formula is as follows:

$$\text{Accuracy} = (TP + TN)/(TP + FP + TN + FN) \quad [14]$$

Precision and Recall sometimes contradict each other, so they need to be considered comprehensively. The most common method is F-Measure (also known as F-Score), the formula is as follows:

$$F1 = 2TP/(2TP + FP + FN) \quad [15]$$

MCC is a balanced index, which is mainly used to solve the problem of binary classification. The value range of MCC is between - 1 and 1. When the value is - 1, it means that the predicted result is completely opposite to the actual result. When the value is 0, it means that the random predicted result is better than the predicted result. When the value is 1, it means that the predicted result is consistent with the actual result, the formula is as follows:

$$MCC = \frac{TP \times TN - TP \times FN}{\sqrt{(TP + FP) \times (TP + FN) \times (TN + FP) \times (TN + FN)}} \quad [16]$$

The measurement of clustering performance is also called clustering validity index. For clustering results, we need to use some performance measure to evaluate their quality. On the other hand, if the final performance measurement is defined, it can be directly used as the optimization objective of the clustering process, so as to better obtain the required clustering results. In this paper, we use the FMI index as the evaluation criterion, the formula is as follows:

$$FMI = \frac{TP}{\sqrt{(TP + FP) \times (TP + FN)}} \quad [17]$$

The mean value is the sum of all the values and then

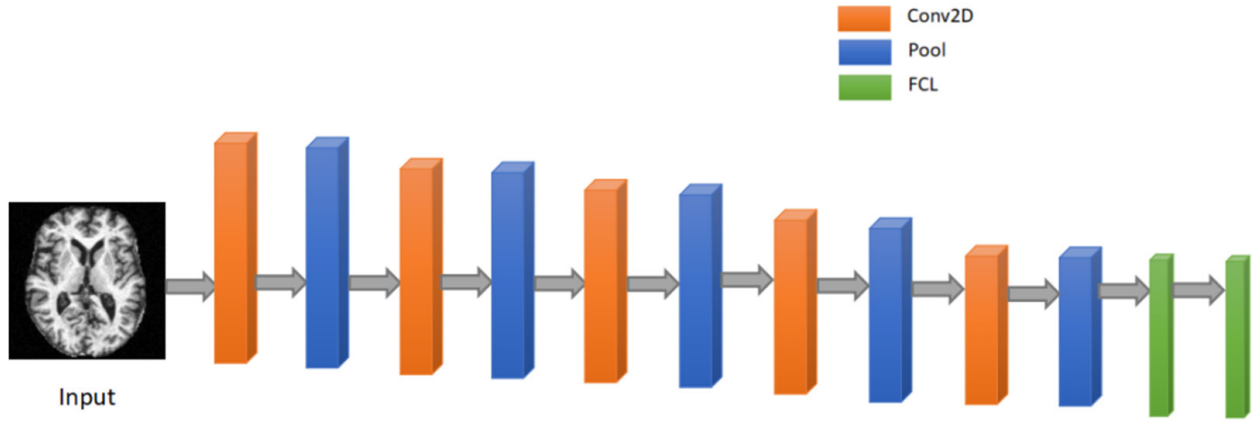

Figure 6. Flow chart.

divided by the number, the formula is as follows:

$$\mu = \frac{1}{n}\sum_{i=1}^{n} y_i \quad [18]$$

Where n is the number of runs and y_i is the results of each run.

The standard deviation (SD) variance reflects the degree of data dispersion, the formula is as follows:

$$SD = \sqrt{\frac{1}{n-1}\sum_{i=1}^{n}(y_i - \mu)^{2}} \quad [19]$$

Experiments

Statistical Analysis

We ran ten operations and got ten sets of data in this paper, as shown in Table 4. We got the highest sensitivity value of 98.25 in the fourth group and the lowest sensitivity value of 92.98 in the tenth group. For the specificity, the highest specificity value of 97.52 in the fourth group to the seventh group and the lowest specificity value of 93.39 in the third and tenth groups. Among the ten groups of data, the highest precision was 97.39 in the fourth group, and the lowest was 92.98 in the tenth group. The highest accuracy was 97.87 in the fourth group, and the lowest was 93.19 in the tenth group. The maximum value of F1 was 97.82 in the fourth group and the minimum value was 92.98 in the tenth group. The maximum value of MCC was 95.75 in the fourth group and the minimum value was 86.37 in the tenth group. The maximum value of FMIS was 97.82 in the fourth group and the minimum value was 92.98 in the tenth group.

As shown in **Figure 7**, it can be concluded that the fourth group of data results were the best, and all the values were the highest in the ten groups of data. The result of the tenth group was the worst and all the values were the lowest among the ten groups of data.

Comparison to State-of-the-art

In order to verify the effectiveness of the proposed neural network structure, we used four state-of-the-art approaches to conduct comparative experiments, HMI (4), 3SEJ (5), CSO (6) and LRC (7). The comparison test results are shown in Table 5. For the sensitivity, our method got the highest sensitivity value (95.96). For the specificity, the highest value of specificity was 95.95 from our method. Compared with four state-of-the-art approaches, our method got the highest precision value (95.73). The accuracy of our method was the highest, which was 95.96. For the F1, the highest value was 95.84 from our method. The MCC value of our method (91.92) was much larger than four state-of-the-art approaches. Our method also got the largest value of FMI (95.84).

As shown in Figure 8, our experimental method is better than four state-of-the-art approaches. All the classification index values we got are better than four state-of-the-art approaches.

Conclusion

With the continuous development of computing, the application of computer technology is more and more widely. In recent years, computer technology has been continuously applied in medicine and obtained a lot of innovation. In this paper, a method of self-diagnosis of

Table 3. confusion matrix.

		Actual class	
		Positive	Negative
Predicted class	Positive	True positive (TP)	False positive (FP)
	Negative	False negative (FN)	True negative (TN)

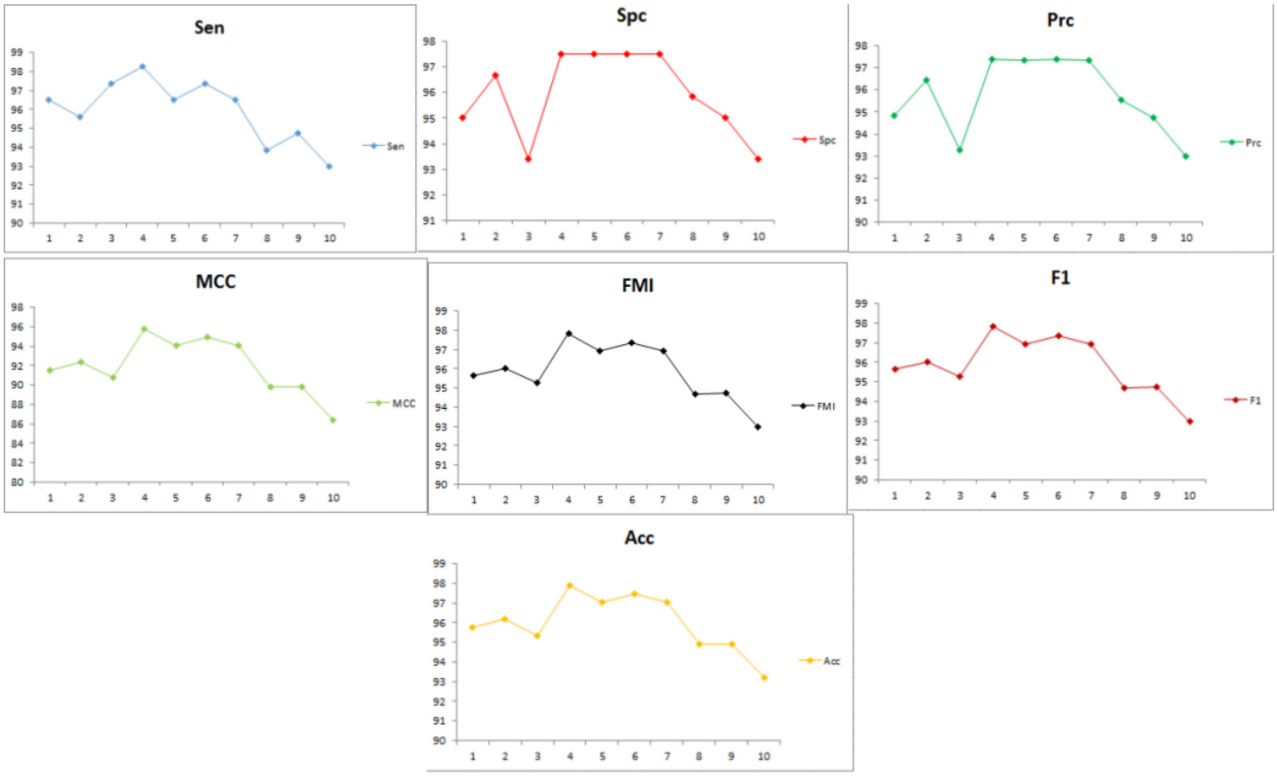

Figure 7. Experimental results.

alcoholism based on 6-layer customized deep convolution neural network was proposed. With 235 participants, the accuracy rate was 95.96% ± 1.44%. The sensitivity, specificity, precision, FI, MCC, and FMI were 95.96% ± 1.66%, 95.95%±1.67%, 95.73% ± 1.72%, 95.84% ± 1.48%, 91.92% ± 2.87%, 95.84% ± 1.48%, respectively. Compared with four state-of-the-art approaches, the results obtained by the proposed neural network structure are more accurate. Therefore, according to its excellent experimental results, the proposed neural network structure in this paper can be used as one of the methods for diagnosing alcoholism.

Even though this paper obtained great data, there are still some shortcomings to be solved in the future. (1) there are only 216 images in this paper. For deep convolution learning, the number of training set and test set is too small. (2) We did not compare the performance of convolution layer and fully connected layer with different number of layers so we did not get the optimal number of convolution and fully connected layers.

In the future work, we will collect more data to do research. Second, we will do more experiments to get the optimal number of convolution and fully connected layers. Finally, we will test more new network technologies.

Conflict of interest

The authors declare that they have no conflicts of interest to disclose.

Table 4. Experimental results.

Run	Sen	Spc	Prc	Acc	F1	MCC	FMI
1	96.49	95.04	94.83	95.74	95.65	91.50	95.66
2	95.61	96.69	96.46	96.17	96.04	92.34	96.04
3	97.37	93.39	93.28	95.32	95.28	90.72	95.30
4	98.25	97.52	97.39	97.87	97.82	95.75	97.82
5	96.49	97.52	97.35	97.02	96.92	94.04	96.92
6	97.37	97.52	97.37	97.45	97.37	94.89	97.37
7	96.49	97.52	97.35	97.02	96.92	94.04	96.92
8	93.86	95.87	95.54	94.89	94.69	89.79	94.69
9	94.74	95.04	94.74	94.89	94.74	89.78	94.74
10	92.98	93.39	92.98	93.19	92.98	86.37	92.98
MSD	95.96 ± 1.66	95.95 ± 1.67	95.73 ± 1.72	95.96 ± 1.44	95.84 ± 1.48	91.92 ± 2.87	95.84 ± 1.48

Table 5. Comparison results.

	Sen	Spc	Prc	Acc	F1	MCC	FMI
HMI (4)	88.86	89.42	88.78	89.15	88.82	78.28	99.82
3SEJ (5)	93.60	93.72	93.35	93.66	93.47	87.31	93.47
CSO (6)	91.84	92.40	91.92	92.13	91.88	84.24	91.88
LRC (7)	91.54 ± 1.47	93.66 ± 1.34	93.45 ± 1.27	92.61 ± 0.81	92.48 ± 0.83	85.26 ± 1.62	92.47 ± 0.84
Ours	95.96 ± 1.66	95.95 ± 1.67	95.73 ± 1.72	95.96 ± 1.44	95.84 ± 1.48	91.92 ± 2.87	95.84 ± 1.48

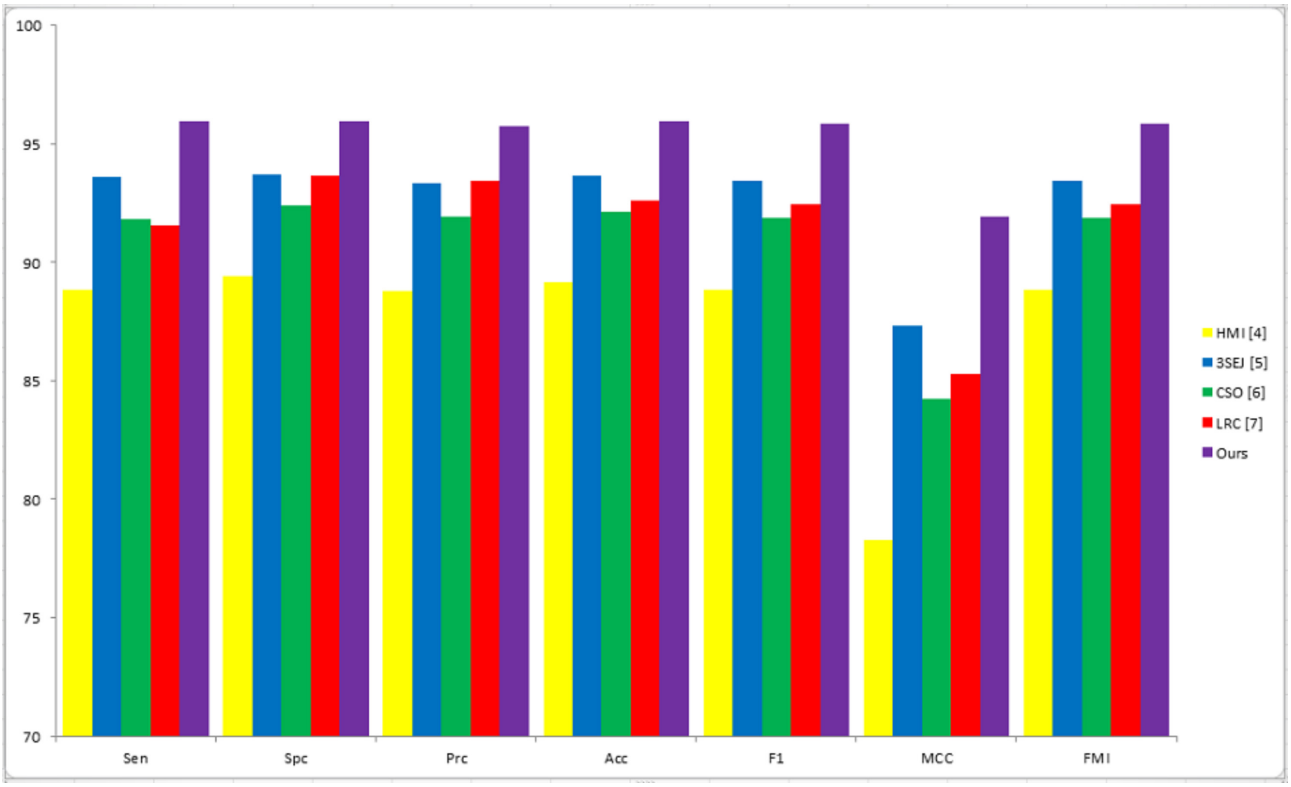

Figure 8. Comparison results.

References

1. Kumar S, Ghosh S, Sinha RK. Using computational classifiers to detect chronic alcoholism. J Clin Eng. 2016;41(2):90-4.
2. Rodrigues JdC, Filho PPR, Peixoto E, N AK, de Albuquerque VHC. Classification of EEG signals to detect alcoholism using machine learning techniques. Pattern Recognit Lett. 2019;125:140-9.
3. Anuragi A, Sisodia DS. Empirical wavelet transform based automated alcoholism detecting using EEG signal features. Biomed Signal Process Control. 2020;57.
4. Hou X-X. Alcoholism detection by medical robots based on Hu moment invariants and predator-prey adaptive-inertia chaotic particle swarm optimization. Comput Electr Eng. 2017;63:126-38.
5. Han L. Identification of Alcoholism based on wavelet Renyi entropy and three-segment encoded Jaya algorithm. Complexity. 2018;2018.
6. Qian P. Cat Swarm Optimization applied to alcohol use disorder identification. Multimed Tools Appl. 2018;77(17):22875-96.
7. Chen X. Alcoholism detection by wavelet eergy entropy and linear regression classifier. Comput Model Eng Sci. 2021;127:325-43.
8. Barik A, Rai RK, Chowdhury A. Alcohol use-related problems among a rural indian population of west bengal: an application of the alcohol use disorders identification test (AUDIT). Alcohol Alcohol. 2016;51(2):215-23.
9. Wang S-H, Muhammad K, Lv Y, Sui Y, Han L, Zhang Y-D. Identification of alcoholism based on wavelet Renyi entropy and three-segment encoded jaya algorithm. Complexity. 2018;2018:1-13.
10. Woolrich MW, Jbabdi S, Patenaude B, Chappell M, Makni S, Behrens T, et al. Bayesian analysis of neuroimaging data in FSL. Neuroimage. 2009;45(1 Suppl):S173-86.
11. Smith SM, Jenkinson M, Woolrich MW, Beckmann CF, Behrens TE, Johansen-Berg H, et al. Advances in functional and structural MR image analysis and implementation as FSL. Neuroimage. 2004;23 Suppl 1:S208-19.
12. Albawi S, Mohammed TA, Al-Zawi S, editors. Understanding of a convolutional neural network. International Conference on Engineering and Technology; 2017; Akdeniz Univ, Antalya, TURKEY: IEEE.
13. Lv Y-D. Alcoholism detection by data augmentation and convolutional neural network with stochastic pooling. J Med Syst. 2018;42(1).

14. Tang C. Twelve-layer deep convolutional neural network with stochastic pooling for tea category classification on GPU platform. Multimed Tools Appl. 2018;77(17):22821-39.
15. Ahmed HOA, Nandi AK. Connected components-based colour image representations of vibrations for a two-stage fault diagnosis of roller bearings using convolutional neural networks. Chin J Mech Eng. 2021;34(1):21.
16. Pan C. Abnormal breast identification by nine-layer convolutional neural network with parametric rectified linear unit and rank-based stochastic pooling. J Comput Sci. 2018;27:57-68.
17. Pan C. Multiple sclerosis identification by convolutional neural network with dropout and parametric ReLU.J Comput Sci. 2018;28:1-10.
18. Nguyen H, Tran T. Three-dimensional shape reconstruction from single-shot speckle image using deep convolutional neural networks. Opt Lasers Eng. 2021;143:10.
19. Krizhevsky A, Sutskever I, Hinton GE. ImageNet classification with deep convolutional neural networks. Commun ACM. 2017;60(6):84-90.
20. Zhao G. Polarimetric synthetic aperture radar image segmentation by convolutional neural network using graphical processing units. J Real Time Image Process. 2018;15(3):631-42.
21. Huang C. Multiple sclerosis identification by 14-layer convolutional neural network with batch normalization, dropout, and stochastic pooling. Front Neurosci. 2018;12.
22. Mariani S, Rendu Q, Urbani M, Sbarufatti C. Causal dilated convolutional neural networks for automatic inspection of ultrasonic signals in non-destructive evaluation and structural health monitoring. Mech Syst Signal Proc. 2021;157:22.
23. Muhammad K. Image based fruit category classification by 13-layer deep convolutional neural network and data augmentation. Multimed Tools Appl. 2019;78(3):3613-32.
24. Xie S. Alcoholism identification based on an AlexNet transfer learning model. Front Psychiatry. 2019;10.
25. Rogers MSJ, Bithell M, Brooks SM, Spencer T. VEdge_ Detector: automated coastal vegetation edge detection using a convolutional neural network. Int J Remote Sens. 2021;42(13):4809-39.
26. Deshpande P, Belwalkar A, Dikshit O, Tripathi S. Historical land cover classification from CORONA imagery using convolutional neural networks and geometric moments. Int J Remote Sens. 2021;42(13):5148-75.
27. Wang S-H. DenseNet-201-based deep neural network with composite learning factor and precomputation for multiple sclerosis classification. ACM Trans Multimedia Comput Commun Appl. 2020;16(2s):Article 60.
28. Sangaiah AK. Alcoholism identification via convolutional neural network based on parametric ReLU, dropout, and batch normalization. Neural Comput Appl. 2020;32:665-80.
29. Dalal S, Khalaf OI. Prediction of occupation stress by implementing convolutional neural network techniques. J Cases Inf Technol. 2021;23(3):27-42.
30. Zhang Y-D, Dong Z-C. Advances in multimodal data fusion in neuroimaging: Overview, challenges, and novel orientation. Inf Fusion. 2020;64:149-87.
31. Wang S-H. Covid-19 Classification by FGCNet with deep feature fusion from graph convolutional network and convolutional neural network. Inf Fusion. 2021;67:208-29.
32. Peker M. Classification of hyperspectral imagery using a fully complex-valued wavelet neural network with deep convolutional features. Expert Syst Appl. 2021;173:11.
33. Satapathy SC. A five-layer deep convolutional neural network with stochastic pooling for chest CT-based COVID-19 diagnosis. Mach Vis Appl. 2021;32.

RESEARCH ARTICLE

Isolation and characterization of DNA barcodes from distinctive and rare terrestrial animals in China using universal *COI* and *16S* primers

Mali GUO[a,b,#], Zhenzhen PENG[a,b,#], Xiaoting ZHANG[a,b,#], Chaohai YUAN[a,b], Hanxi LU[a,b], Keyun ZHANG[d], Yafei CAI[a,b,*], Wei ZHANG[a, b,*]

[1] *College of Animal Science and Technology, Nanjing Agricultural University, 210095 Nanjing, China*
[2] *National Experimental Teaching Demonstration Center of Animal Science, Nanjing Agricultural University, 210095 Nanjing, China*
[3] *College of Life Science, Nanjing Agricultural University 210095 Nanjing, China*

[#] These authors contribute equally.
*Correspondence: weizhang@njau.edu.cn, ycai@njau.edu.cn
https://doi.org/10.37175/stemedicine.v2i7.95

ABSTRACT

Background: Accurate taxonomic identification is the cornerstone for monitoring, conservation and management of ecological resources. China has the highest biodiversities and the richest species assemblages in the world, but is lacking in sufficient assessment to the abundant genetic variability. DNA barcoding is a proven tool employing sequence information for rapid and unambiguous species delineation. However, the ability of barcodes to distinguish species that are archaic and distinctive evolutionary lines remains largely untested.

Methods: In order to investigate the resources of terrestrial animals in China, regions from mitochondrial *COI* and *16S* are barcoded for 395 specimens belonging to 54 selected species, many of which are indigenous representatives in danger. High success rate of PCR amplification is achieved by using universal *COI* and *16S* primers with many *numts* pseudogenes co-amplified from mammalian samples.

Results: Application of barcodes to flag species is generally straightforward since no *COI* or *16S* haplotypes are shared between closely related species. Barcoding gap, species resolution and phylogenetic relationships relying on our barcode libraries are further compared using distance and tree based approaches.

Conclusion: Results show that the discriminatory power of the two barcode markers could differentiate on a case-by-case basis, and also suggest a careful consideration of the nuclear numts for barcoding studies as they might provide a new understanding for evolution.

Keywords: DNA barcode · *COI* · *16S* · Indigenous animals · China

Introduction

China is among the highest biodiversities and has the richest species assemblages in the world. It is estimated that over 10% of the world's ecosystem types exist in this country, including ~2485 species of terrestrial vertebrates and at least 51,000 species of insects identified already (1). This species richness definitely is still underestimated as the rate of new and cryptic species discovery remains high. However, China's genetic resources have also decreased sharply in the past decades due to its large human population and intensive human activities (2). Nearly half of China's animals are found nowhere else and many are archaic and distinctive evolutionary lines nowadays at serious risk of extinction, such as the Giant panda (*Ailuropoda melanoleuca*) and Chinese alligator (*Alligator sinensis*) (3). Consequently, the high rates of

Received: June 1, 2021; Accepted: June 11, 2021.

species discovery and loss have led to the urgent need for standardized methods to assess varied animal groups.

Conventional taxonomic approaches for classification of species or breeds mainly rely on the characterization of morphological features, which are time-consuming and in some cases even lead to the disappearance of a species before its description (4). Moreover, both genetic and environmental factors underlie morphological variations. How genetic and environmental factors influence morphological characteristics remains a fundamental question under biological investigations (5). Observations based on morphology thereby are often unclear and challenging for species discovery and delimitation. Although whole genome sequencing and mass spectrometry-based protein profiling have also emerged as high throughput techniques allowing more precise species and breeds assessment (6, 7), the tedious analysis and high price slow their development in the field and, as a result, faster and easier alternatives with low costs are preferred.

DNA barcoding is a molecular tool employing sequence divergence in short and standardized gene regions to aid identification and discovery of species (8). It seeks to adopt one or few DNA fragments to efficiently and effectively assign any biological sample to its species regardless of the visual identification of the sample (9). The core idea is based on the fact that certain pieces of DNA, when aligned, can be found to vary merely to a limited degree within species while this variation is much less than between species (10). Therefore, whether samples of diverse species can be differentiated largely depends on the choice of the DNA sequence, which should be easy for amplification using universal PCR primers. Regions from mitochondrial genes usually form barcodes for members of animal kingdom. This is because each mitochondrion possesses insufficient DNA repair mechanisms and multiple copies of naked DNA without the protection of histone proteins, resulting in a 10-fold higher rate of nucleotide substitution in comparison to nuclear genome (11, 12). The accumulation of mutation in mitochondrial DNAs (mtDNAs) helps introduce more sequence diversity to establish phylogenetic relationships among animals and increases the chance to distinguish between closely related species (13).

A short fragment of ~648 base pairs (bp) at the 5' end of the mitochondrial gene encoding the cytochrome c oxidase subunit 1 (*COI*) enzyme is the first and so far the most broadly used molecular marker for barcoding animals (14). It was reported that more than 95% of species in test assemblages of different animal groups, mainly insects, birds and fishes, showed characteristic *COI* sequences after successfully amplified using a universal pair of primers (15). More studies, however, challenged the degree of universality for *COI* and its primers for a number of reasons. For instance, the high variability of nucleotide sequences at the *COI* priming sites hinders its application to a broader spectrum of animal species (16). To address this issue, selected *COI* region and primers have been modified for barcoding species like amphibians (17). Yet how well the modifications work for bio-identification of other animals is still questionable, especially when coming to some distinctive and rare lines. As an alternative candidate, mitochondrial *16S ribosomal RNA* gene is also often used, but its usage is substantially restricted to simple taxonomic analyses of microbiota (18). This is because of the prevalence of insertions and deletions in the non-coding RNA, which is thought to greatly complicate sequence alignments, although successes that *16S* is superior to *COI* are also realized recently for Arthropoda and Amphibians (13, 19, 20). In spite of this, whether *16S* could supply a sufficient resolution and robustness to discover entire animal kingdom has not been fully explored.

To date, little is known about the effectiveness of DNA barcode for evaluating taxonomic and phylogenetic structures of rare indigenous animals. In the paper present here, we select 54 representative species of distinctive terrestrial animals with 395 samples collected in 15 provinces throughout China, and systematically test the recovery of sequence information with universal primer sets that target short segments of the *COI* and *16S* barcode regions. The goal of this work focuses on the prospect for investigating the genetic variability of threatened species using barcode sequences of *COI* and *16S* through both distance-based and tree-based approaches. Our efforts will assist policy makers to understand the global patterns of biodiversity and persuade them to develop management strategies for prioritization and hot spots for conservation.

Materials and Methods

Sample acquisition

Animal samples including blood, semen, hair, tissues and faeces were collected in P. R. China following Animal Use Protocols approved by the Animal Care and Ethics Committee of Nanjing Agricultural University. Geographical distribution map of sample collection sites was created by making use of HyperText Markup Language 5 (HTML 5) and JavaScript scripting language (**Figure 1**). Blood samples were preserved with EDTA, whereas semen and faecal samples were frozen in liquid nitrogen. Hairs and tissues were kept in 75% ethanol. Species identity was based on morphological characters determined in the field. A total of 395 specimens representing 54 animal species, including 14 indigenous breeds of farm animals (4 species) in China, were used in this study (Supplemental **Table S1**). Some species were rare and represented by a single specimen solely, but for the majority multiple specimens were analyzed.

DNA extraction

DNA from blood samples was extracted using TINAamp Blood DNA Kit (DP348-03), while TINAamp Genomic DNA Kit (DP304-02) was adopted for DNA extraction from tissues. DNA from animal semen was purified using

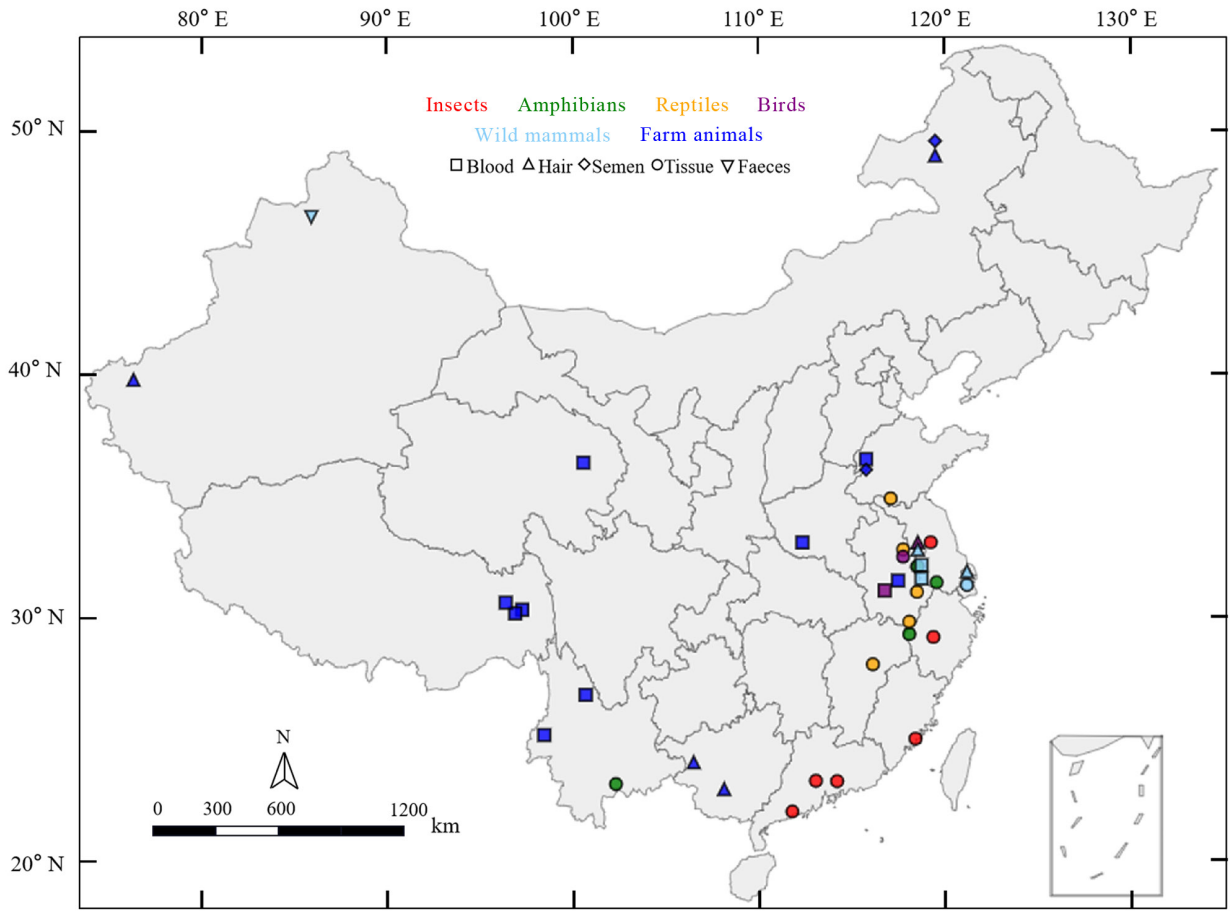

Figure 1. Map of China with sampling sites indicated according to the classification and properties of the specimens. Detailed sample information is shown in Table S1.

Omega Forensic DNA Kit (D3591-02), and Omega Stool DNA Kit (D4015-01) was applied for camel faecal samples. All procedures were carried out according to the manufacturer's protocol. DNA concentration and purity were assessed by Thermo Fisher Scientific NanoDrop One. DNA from animal hairs was extracted using alkaline lysis method as mentioned in (21). In brief, hair follicles from 10 hairs were boiled in 50 µL 0.2 M NaOH for 15 min, and 50µL Tris-HCl (pH = 6.0) was then added before following experimental performance.

COI and *16S* amplification

Less than 150 ng DNA or 5 µL hair lysate was used as template to amplify mitochondrial *COI* and *16S* fragments. PCR was carried out in a 50 µL volume reaction using a Taq DNA polymerase (Vazyme, P213) with proofreading activity. Two sets of primers, COI-C0 and Chm4 (**Table 1**), were used depending on species to

Table 1. Sequence information of universal PCR primers for *COI* and *16S*.
Base pairs underlined indicate 2-fold degenerate bases.

Barcode	Primer	Name	Primer sequence 5'--3'	Source
COI	COI-C0	COI-C02	AYTCAACAAATCATAAAGATATTGG	[1]
		COI-C04	ACYTCRGGRTGACCAAAAAATCA	
	Chm4	Chmf4	TYTCWACWAAYCAYAAAGAYATCGG	[1]
		Chmr4	ACYTCRGGRTGRCCRAARAATCA	
16S	16S	16Sar-L	CGCCTGTTTATCAAAAACAT	[2]
		16Sbr-H	CCGGTCTGAACTCAGATCACGT	

[1] CHE, J., CHEN, H. M., YANG, J. X., JIN, J. Q., JIANG, K., YUAN, Z. Y., MURPHY, R. W. & ZHANG, Y. P. 2012. Universal COI primers for DNA barcoding amphibians. Mol Ecol Resour, 12, 247-58.
[2] PALUMBI, S. J. D. O. Z. & HAWAII, K. M. L. U. O. 1991. Simple fool's guide to PCR. Dept of Zoology & Kewalo Marine Laboratory University of Hawaii.

amplify the same barcoding region of *COI* (17). *16S* barcoding region was amplified with 16Sar-L and 16Sbr-H primers (**Table 1**) by using 1.2 μM of each for all species (22). PCR products were visualized on 1% (w/v) agarose gels with ethidium bromide and recovered using TIANgel Midi Purification Kit (DP209). Details of PCR conditions and products for each sample are shown in Supplemental **Table S2**.

TA cloning

Purified PCR products were linked to pMD19-T vector with pMD™19-T Vector Cloning Kit (TaKaRa 6013) in a 10μL reaction containing 4.75 μL PCR product, 0.25 μL vector and 5 μL Solution I. The mixture was incubated at 16 ℃ for 30 min and then transformed into DH5α competent cells (Vazyme, C502) according to the instruction. After gentle mixing, competent cells were placed on ice for 30 min, and then in 42 ℃ water bath for 45s before quick transfer into ice for 3 min. Bacteria were cultivated in 100 μL LB media at 37 ℃ for 10 min and spread on LB agar plates containing 0.1mg/mL ampicillin, 0.04 mg/mL X-gal and 25 μg/mL IPTG for selection. Single white colonies were picked up and cultivated for sequencing.

Sanger sequencing

DNA barcoding regions were sequenced on both directions using PCR primers directly for PCR products, or using RV-M: GAGCGGATAACAATTTCACACAGG and M13F-47: CGCCAGGGTTTTCCCAGTCACGAC primers for TA clonings. The number of colonies sequenced is in line with one colony per 50 bp of barcoding region unless identical barcode sequence was sequenced twice. Sequencing results were assembled, aligned and annotated using DNASTAR Lasergene package before manually checked. All gained sequences were confirmed by sequence similarity search available in GenBank and deposited under the following accession numbers: MZ046006-MZ046047, MZ046083-MZ046118, MZ046726-MZ046731, MZ047098-MZ047179, MZ048967-MZ049527, MZ050069-MZ050116, MZ050118-MZ050213, MZ050493-MZ050515, MZ061667-MZ061700, MZ068220-MZ068223, MZ098871-MZ099441, MZ099449-MZ099455 for *COI* sequences; MZ031856-MZ031915, MZ040165-MZ040224, MZ040226-MZ040319, MZ040322-MZ040403, MZ040406-MZ040487, MZ040500-MZ040596, MZ040600-MZ040754, MZ040922-MZ041011, MZ041035-MZ041093, MZ041115-MZ041206, MZ042146-MZ042231, MZ042371-MZ042467, MZ042537-MZ042621, MZ042714-MZ042791, MZ042801 and MZ061594-MZ061630 for *16S* sequences.

Sequence diversity

DNA Sequencing Polymorphism (DnaSP) was adopted to screen for haplotypes and polymorphic sites by moving a 200-bp-long sliding window 1 bp at a time, and to calculate haplotype diversity (Hd), nucleotide diversity (π) and the average number of nucleotide differences (K). Parameters regarding the length and composition of DNA and protein sequences were determined by MEGA X. Translations of *COI* haplotypes were checked via EditSeq with codon usage and isoelectric point calculated automatically using genetic codes for mitochondrial DNA.

Distance and Tress matrices

DNA or protein sequences were aligned by the Clustal W method before the following bioinformatic calculations contained in the software package of MEGA X. Inter/intraspecific genetic distance for *COI* and *16S* was plotted using the R programming language based on Kimura's 2-parameter (K2P) model. K2P is one of the optimal theories for small pairwise distances, and is widely used to calculate sequence divergences in DNA barcoding literatures despite it is criticized (23). For each animal class, the minimum interspecific distance was compared with the maximum intraspecific distance in order to determine the presence or absence of a barcoding gap. Neighbor joining and maximum likelihood trees construction were done using the "pairwise deletion" option for the treatment of gaps and missing data. Node support was computed by 1000 bootstrap replicates with K2P distance for DNA data and Jones-Taylor-Thornton (JTT) algorithms for proteins as a model of substitution. Phylogenetic dendrograms were finally exported into the web based iTOL (https://itol.embl.de/itol.cgi) tool for annotation and visualization.

Statistical analysis

All data are expressed as the average ± SD. Spearman's correlation coefficient was used on data processing to assess the relationship between the variables. Data analysis was performed using the IBM SPSS software. Comparisons between two groups were made using Student's t-test. The level of significance was set at $p < 0.05$.

Results and Discussion

Isolation and characterization of COI DNA barcodes

Both COI-C0 and Chm4 primer sets were reported to span the same positions in the *COI* gene of amphibians (17). The Chm4 primer set was designed to have more 2-fold degenerate bases in comparison to COI-C0 (Table 1). Therefore, the Chm4 primer set is utilized in this study only when the COI-C0 primers fail to amplify a perfect PCR product. In this experimental setting, 1480 *COI* sequences recovered from 391 specimens (> 98.98% success) yield 787 unique haplotypes ranging from 616 to 663 bp with an average of 652 bp, among which 592 haplotypes are defined from 1094 sequences generated by COI-C0 for 28/6 species/breeds, while the rest are from 25/8 species/breeds through Chm4 primer pair (**Figure 2a**, **Supplemental Table S2** *COI* 1st pair and **Table S3**). Notably, haplotype sequences of *COI* are only shared

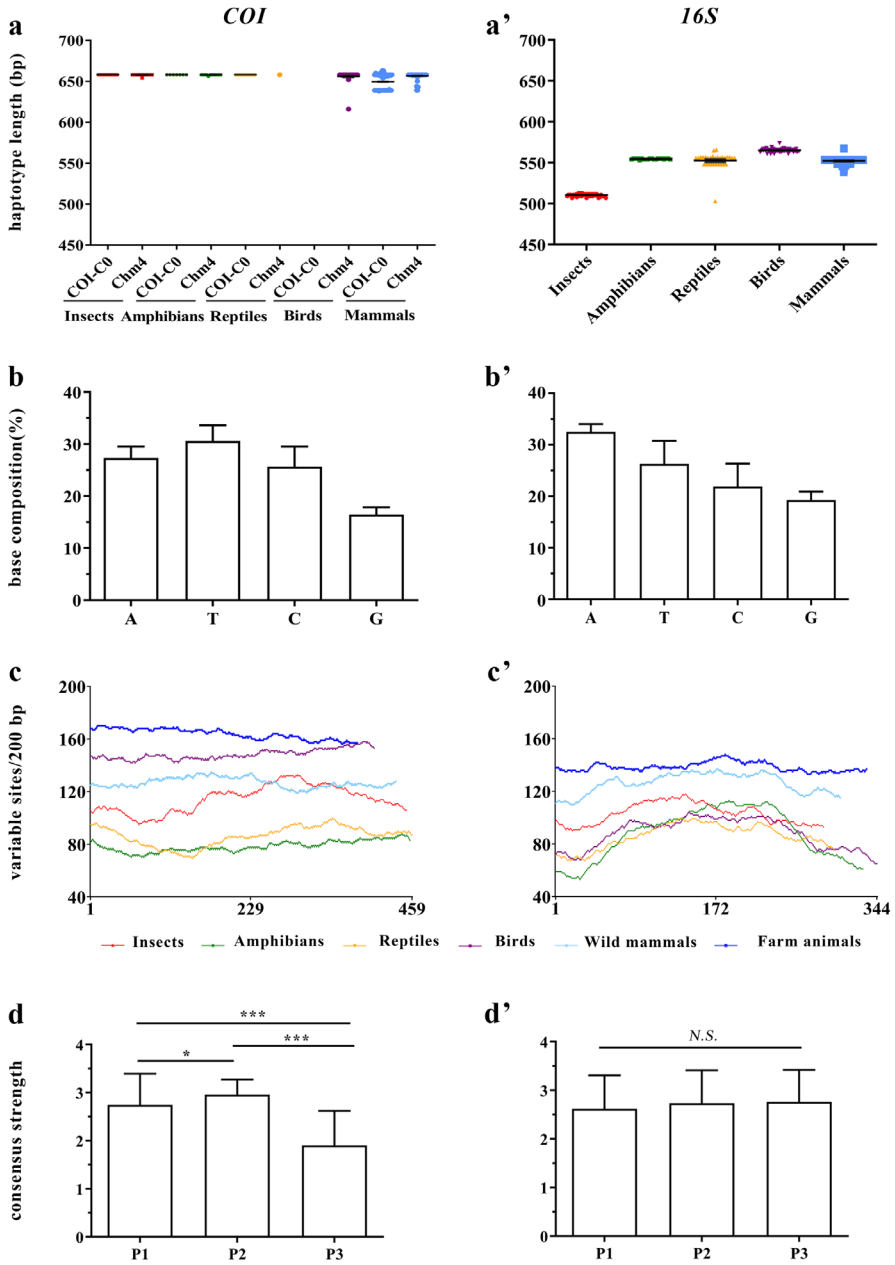

Figure 2. Isolation and characterization of *COI* and *16S* barcodes. (a-b') Sequence length and average nucleotide composition of *COI* (a and b) and *16S* (a' and b') haplotypes. (a and a') Each dot represents a unique haplotype. (c and c') Sliding window graph comparing the number of variable sites for *COI* and *16S* haplotypes. Each window size of 200 bp is slid through the full segment 1 bp at a time, resulting in 459 windows for *COI* (c) and 344 for *16S* (c'). Animal groups are indicated by lines with different colors. (d) Variation of the triplet code of *COI* haplotypes. Consensus strength is scored according to the Alignment Report given by MegAlign using Lasergene software package and plotted according to the positions of genetic code. (*) $p<0.05$; (***) $p<0.001$. The same rules are applied to non-coding *16S* haplotypes but the codon positions are defined randomly (d'). (N.S.) not significant.

among various breeds of farm animals, but not at the level of species.

The average nucleotide composition of *COI* haplotypes is 27.32% A, 30.58% T, 25.65% C and 16.45% G (**Figure 2b**). The GC content of these sequences varies from 25.60% to 52.40%, and identifies insects having the lowest GC content, consistent with what was reported before (24). As shown in Figure 2c, the density of variable sites in 200 bp windows along the alignment of *COI* haplotypes does not fluctuate widely for each animal group. Even so, the third position of genetic code generally is the least conserved and the second codon position shows slightly smaller variation than the first position (**Figure 2d**), in line with the "wobble phenomenon" during protein translation (25). However, this is not the case for *16S*, which is a non-coding RNA and has all positions varying at an identical rate (**Figure 2d'**).

Isolation and characterization of 16S DNA barcodes

The 16S primers manage to obtain 1255 sequences from 390 out of 395 collected samples comprising 53/14 species/breeds in this study (**Supplemental Table S2**).

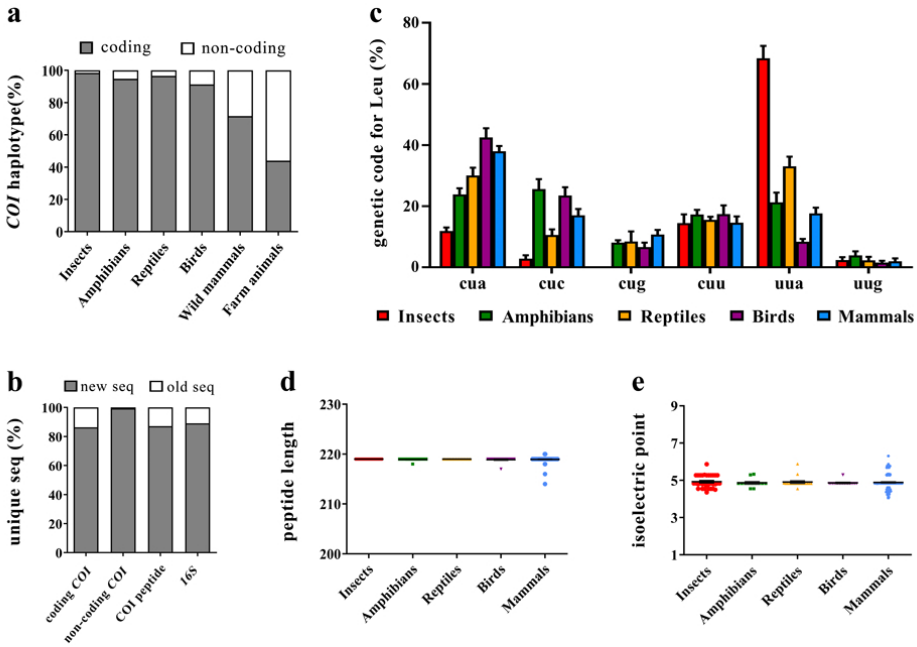

Figure 3. Isolation and characterization of COI peptides. (a) Translation of *COI* haplotypes using genetic codes for mitochondrial DNA among different animal groups as indicated. (b) Percentage of novel sequences (seq) identified after BLAST similarity search in Genbank. (c) Usage of synonymous codons for leucine in COI peptides. Animal classes are indicated by various colors. (d and e) Sequence length and isoelectric point of COI peptides. Each dot represents a unique protein sequence.

After removal of identical sequences within any one species, the barcode library is reduced to 592 unique haplotype segments with an average of 550 bp and lengths ranged from 503 to 574 bp (**Figure 2a'** and **Supplemental Table S4**). Of these, 89.02% haplotypes are newly discovered in current study after aligned to the *16S* sequences in GenBank database. Similar to *COI* barcodes, there is no haplotype sequence of *16S* found to be shared between species either.

The base compositions of *16S* are always biased towards A and T, which together are present in a higher proportion than GC, while the latter varies from 20.70% to 49.38% (**Figure 2b'**). As usual, insects have the lowest GC content. Molecular diversity indices of both *COI* and *16S* barcodes are given in **Table 2** for comparison. Overall, *16S* shows lower nucleotides diversities (π) as well as average number of nucleotide differences (K) for all animal groups when compared with *COI*. Also distinct from *COI*, *16S* haplotypes seem less polymorphic in their initial and final portions for all animal groups except for farm animals, which have the largest amount of variable sites owing to having too many *16S* haplotypes for test (**Figure 2c'**).

Isolation and characterization of COI protein peptides

Translation of *COI* haplotypes is also examined as *COI* is a protein-coding gene with essential function for oxidative phosphorylation (26). Results reveal that out of 787 unique *COI* barcodes, only 462 consisting of 51/11 species/breeds are functional domains containing no stop codon (**Supplemental Table S3**). Of those nonsense mutant fragments, more than 99% are novel sequences, majority of which are derived from mammalian samples (wild mammals and farm animals) (Figure 3a and b). In this respect, the percentage of new *COI* haplotypes able to encode proteins is >13% lower (86.36%), close to that of *16S* (89.02%) when aligned to the data in GenBank.

The 462 functional *COI* barcodes mentioned above in total isolate 318 unique peptides, for all of which Leucine is the amino acid used most frequently although obvious codon bias for Leucine is observed among animal groups (**Supplemental Table S5** and **Figure 3c**). The average length of the 318 COI peptides is 219 amino acids, within a narrow range from 214 to 220 amino acids, correlated with the small window of their isoelectric points between 4.059 and 6.308 (**Figure 3d** and **e**). When compared to data available in Genbank, around 87.11% peptides are characterized to be novel COI sequences (**Figure 3b**). However, sharing of peptide sequence is detected between species of not closely related birds or mammals, indicating COI proteins, in contrast to *COI* nucleotides, possess higher conservatism in the course of species evolution (**Supplemental Table S5**).

Barcoding gap and Species resolution

The primary application of barcode markers is to discriminate species. Methodological approaches for species delineation using DNA barcodes are commonly dependent on genetic distance-based measures, which rely on the assumption of a remarkable separation between intraspecific variation and interspecific divergence in the selected marker, also referred to as the barcoding gap (27, 28). K2P analysis thus is conducted using *COI* haplotypes, coding *COI* and *16S* haplotypes to calculate

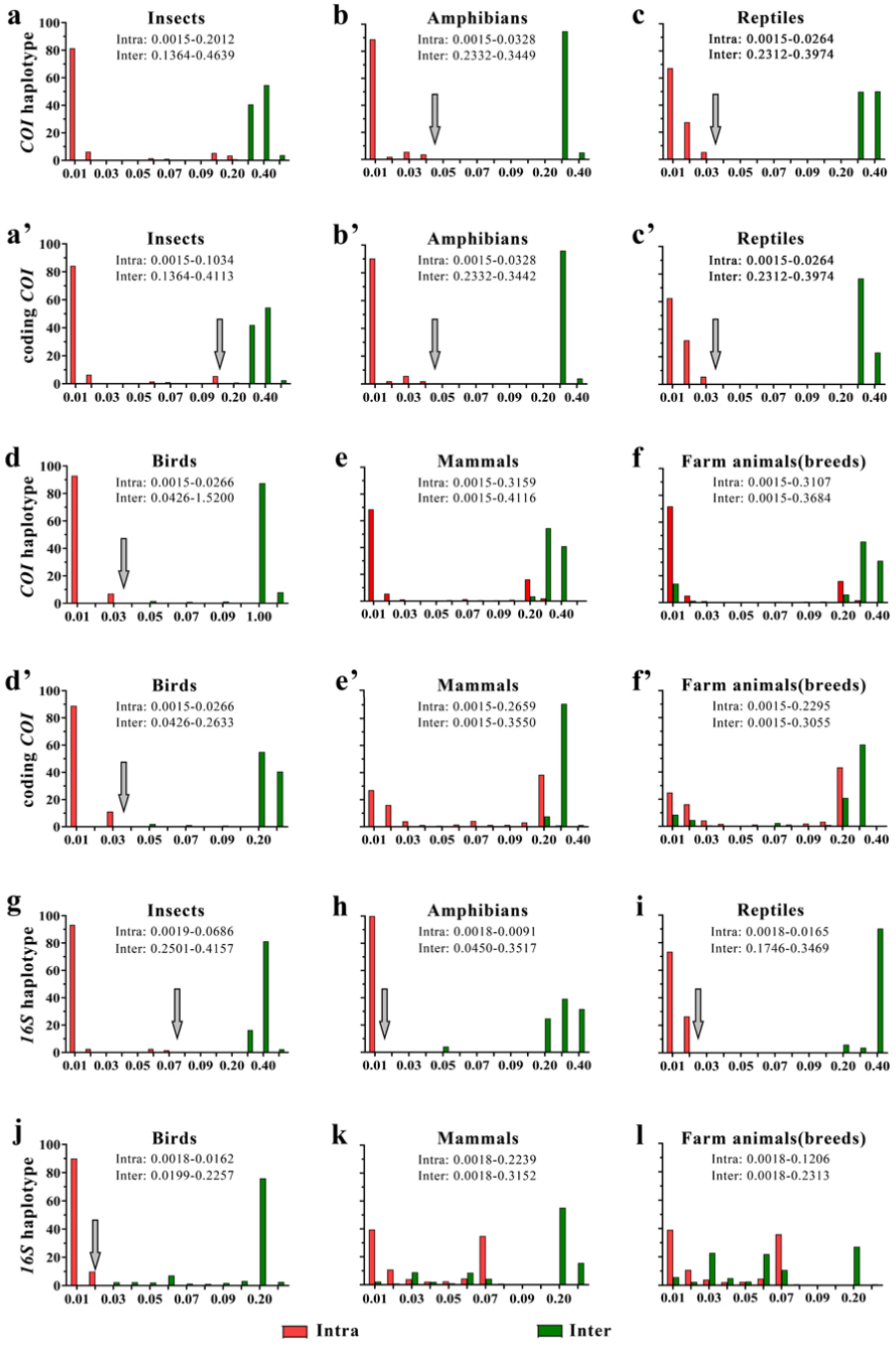

Figure 4. Histograms displaying the intraspecific and interspecific K2P pairwise sequence divergences for all *COI* haplotypes (a-e), coding *COI* (a'-e') and all *16S* haplotypes (g-k) of animal classes as indicated. Genetic distances are also compared within and between the 14 breeds of farm animals with *COI* haplotypes (f), coding *COI* (f') and *16S* (l) haplotypes. The minimum and maximum inter/intraspecific distance is depicted for each comparison. Gray arrows indicate the existence of barcoding gaps.

genetic distance respectively. The two *COI* datasets give comparable outcomes among all animal groups except for insects, in which coding *COI* is moderately better, displaying a murky gap with the minimum interspecific distance higher than the maximum intraspecific distance (**Figure 4a-f'**). Additionally both translatable *COI* and *16S* haplotypes exhibit barcoding gaps for insects, amphibian, reptiles and birds, even though COI protein peptides are shared between some birds (**Figure 4** and **Supplemental Table S5**). Nevertheless, both fail to show a separate distribution for mammals within and between species or breeds (**Figure 4e-f'**).

Sequence datasets then are further evaluated using BLAST searches, which typically employ distance-based algorithms for pairwise alignments to assess species resolution (6). Performance of BLAST using COI peptides no surprise deliver the lowest species resolution because of the highest degree of sequence conservation (**Figure 5a** and **Supplemental Table S5**). As for DNA barcodes, *COI* overall offers better species resolution than *16S* (**Figure 5a**),

Table 2. Genetic diversity of *COI* and *16S* barcodes generated in the present study.

Species	barcode	N	S	H	Hd (SD)	π (SD)	K
Insects	*COI*	138	363	62	0.9240 (0.0120)	0.19422 (0.00208)	126.246
	16S	122	247	51	0.9010 (0.0160)	0.18603 (0.00507)	90.412
Amphibians	*COI*	37	261	19	0.9350 (0.0220)	0.16619 (0.01298)	108.853
	16S	42	194	20	0.9360 (0.0180)	0.15242 (0.00657)	80.632
Reptiles	*COI*	78	308	35	0.9050 (0.0210)	0.15734 (0.00861)	103.528
	16S	69	213	30	0.8880 (0.0270)	0.14312 (0.00722)	70.987
Birds	*COI*	54	448	26	0.9590 (0.0100)	0.18004 (0.02340)	108.92
	16S	69	213	44	0.9740 (0.0090)	0.09766 (0.00357)	53.030
Wild Mammals	*COI*	270	405	157	0.9847 (0.0028)	0.20079 (0.00152)	127.703
	16S	236	297	121	0.9775 (0.0038)	0.12394 (0.00193)	62.465
Farm animals	*COI*	903	474	488	0.9610 (0.0041)	0.14981 (0.00229)	86.592
	16S	717	368	326	0.9666 (0.0027)	0.05204 (0.00205)	27.684

N=number of sequences; S=number of polymorphic sites; H=number of haplotypes; Hd (SD)=haplotype diversity (standard deviation); π (SD)=nucleotide diversity (standard deviation); K=average number of nucleotide differences.

especially for insects, amphibians, reptiles and wild mammals (**Figure 5b**). Although the capability to make species-level identifications diverges tremendously for both DNA markers, a statistically significant correlation (rho = 0.76, $p < 0.01$) is noted between the average resolutions of *COI* and *16S* for each species or breed of farm animals (**Figure 5c**, **Supplemental Table S3** and **S4**). In addition, BLAST results give a general impression that translatable *COI* barcodes have higher levels of species discrimination than their non-coding counterparts (**Figure 5a**). However, this is not always true since for species or breeds such as Golden monkey (*Rhinopithecus roxellanae*), Tibetan cattle (*Bos grunniens*), Sanhe horse and Tibetan horse (*Equus caballus*), some non-functional counterparts can perform even better (**Supplemental Table S3**).

Phylogenetic relationships

Contrary to divergence-based barcoding gap, construction of evolutionary trees places emphasis on conservation areas which are designed or prioritized according to their phylogenetic diversity (29). The most popular approaches to reconstruct phylogenies are the neighbor-joining (NJ) and the maximum likelihood (ML) algorithm. Although both phylogram constructions could correctly discriminate most *COI* haplotypes, with exception discussed below, NJ turns out to act better in light that it allocates related species closer to each other as hinted by the line colors representing animal classes in **Figure 6**. Yet the topologies of ML tree search sometimes can be more similar to the traditional taxonomic classifications. For example, rather than directly rooted from the same node as Sika deer (*Cervus nippon*) (**Figure 6a**),

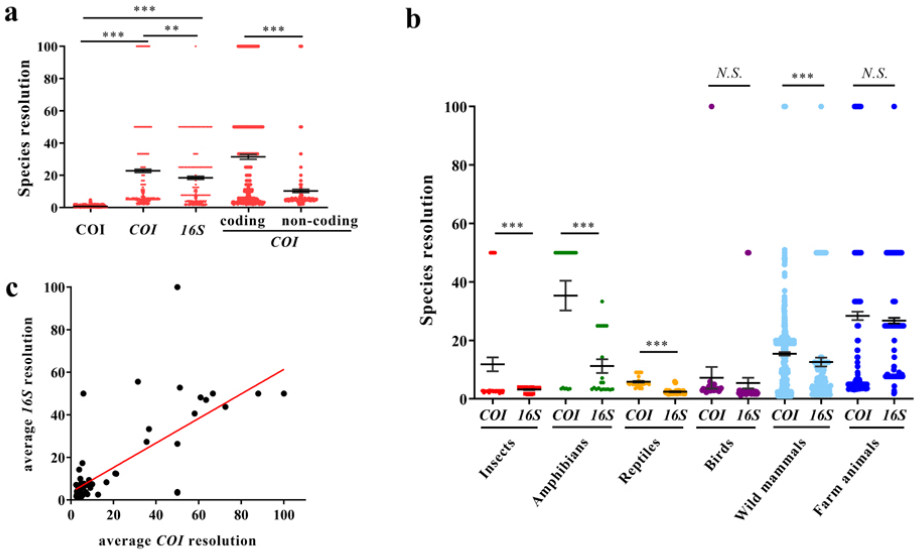

Figure 5. Species resolution provided by *COI*, *16S* DNA barcodes and COI peptides (a) for different animal groups (b) as indicated. Species resolution of unique sequences is predicted using BLAST searches based on reference libraries in Genbank, where reference sequences might be deposited unequally for various species. (**) p<0.01; (***) p<0.001; (N.S.) not significant. (c) Correlation between the average resolutions of *COI* and *16S* for each species or breed of farm animals. Each dot is plotted according to the average values of resolution from all *COI* or *16S* haplotypes belonging to the same species or breed. Spearman's correlation coefficient rho=0.76 (p<0.01).

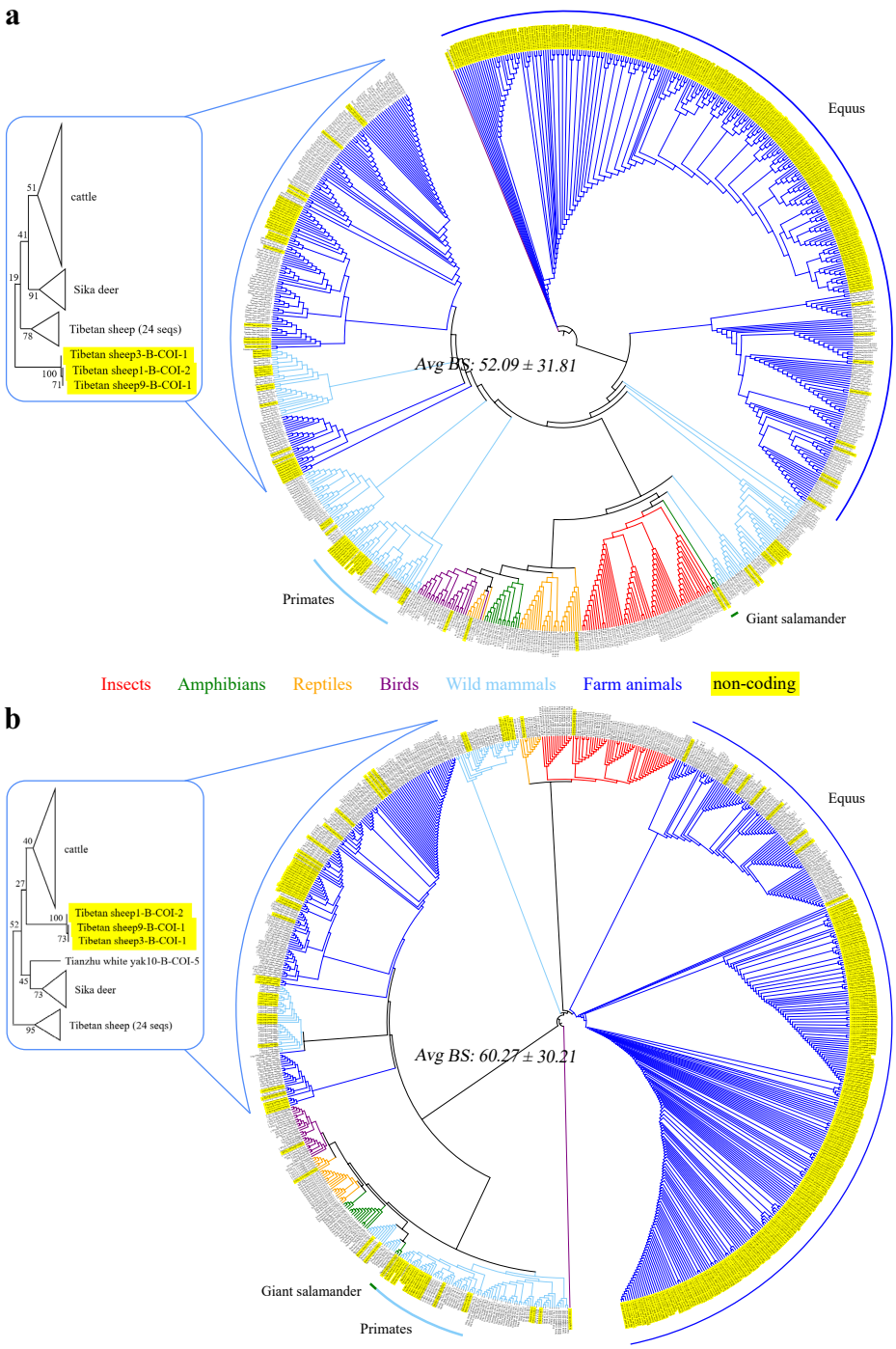

Figure 6. NJ (a) and ML (b) trees inferred from *COI* haplotypes using K2P distances. Highlighted boxes show a more detailed view of Sika deer, Tibetan sheep and cattle with bootstrap values. Sequences from Giant salamander, primates and Equus (horse and donkey) are also highlighted. (Avg BS) average bootstrap support.

COI coming from cattle gather together and form a parallel branch with sheep before grouping with the branch containing deer according to the ML inference (**Figure 6b**). Unexpectedly, the Tibetan sheep (*Ovis aries*) haplotypes here are sequences bearing stop codons and considered as outgroup from the other 24 *COI* barcodes of sheep, whereas one coding sequence from Tianzhu white yak (cattle) is still misplaced with deer (**Figure 6b** box), highlighting a stronger discriminatory power of nonsense mutants that is usually ignored as reviewed by earlier studies (30, 31). Exceptional case common for both tree-building methods is Giant salamander (*Andrias davidianus*), whose coding peptides also fail to cluster with other Amphibians in protein phylogenies based on the JTT models (**Supplemental Figure S1**), indicating a special position of the archaic species in the evolutionary history (32).

It is noticeable that the NJ approach is much more superior to ML when it comes to *16S* haplotypes (**Figure 7**). The average bootstrap proportion of NJ somehow is a little

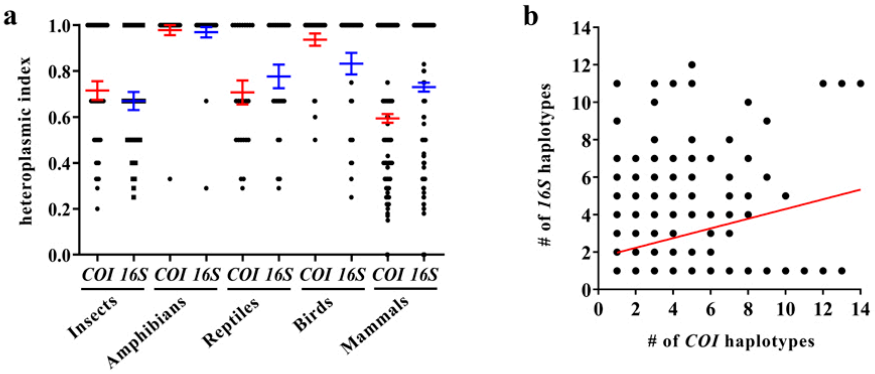

Figure 8. Heteroplasmic conditions in mitochondrial *COI* and *16S* markers. *COI* and *16S* are sequenced directly using PCR primers or after TA cloning, from which bacterial colonies are picked up in line with one colony per 50bp DNA unless the same sequence is captured twice. Heteroplasmy then is monitored either by the chance to obtain identical sequence ("heteroplasmic index" in a) or by the copy number of haplotypes generated (b). (b) Correlation between the copy numbers of *COI* and *16S* barcodes for each individual specimen. Spearman's correlation coefficient rho = 0.18 ($p < 0.01$).

bit lower than ML, but the NJ algorithm identifies all animal classes accurately with each individual *16S* nearly perfectly assigned into their right sites. However, some *16S* sequences originated from primates as well as Equus (horse and donkey) are found to be mixed within their groups and not arranged according to their species. These failures are also detected in phylogenetic trees constructed by *COI*, implying they have a very close kinship (**Figure 6**).

Different from the universal bar code consisting of a series of vertical bars that are printed on commercial products, DNA barcodes are genetic markers seeking to use sequence message of any biological sample, regardless of morphological identification of the sample, to address questions relating to taxonomy, ecology and evolution (33). A considerable amount of studies have evaluated the performance of a variety of barcode markers with respect to both their ease of PCR amplification and their capacity to delineate species (34). By making use of previously reported primers, here we manage to amplify and isolate DNA barcodes from nearly all Chinese terrestrial animals sampled. Totally 787 *COI* and 592 *16S* unique haplotypes are characterized in the survey of 54/14 animal species/breeds. Sequences of selected *COI* and *16S* region are shared inside species but not between species with a low GC content on average, which is a typical feature of mitochondrial genome. In general, *COI* markers are longer and more polymorphic than *16S* as reviewed by parameters of nucleotides diversities (π) and average number of nucleotide differences (K) (**Table 2**). These results clearly demonstrate that both *COI* and *16S* primer pairs possess high degree of universality, competent to capture targeting segments efficiently from distinctive and rare lines of insects, amphibians, reptiles, birds and mammals across China.

In terms of choices of segments for barcoding and species diagnosis, DNA sequences that evolve slowly, like ribosomal genes in nucleus particularly, often do not differ among closely related organisms. Conversely, sequences that evolve rapidly may overwrite the traces of ancient affinities, but regularly reveal divergence between closely related species. Overwhelming evidence has suggested that mitochondrial genome is more likely to supply suitable candidate regions for barcoding animals for its maternal inheritance, non-introns and rapid evolution (35, 36). In order to assess the performance of mtDNAs in our context, distance-based and tree-based approaches are utilized to analyze the data libraries of *COI* and *16S* garnered in this study. Substantially, all methods tend to be congruent with regards to success or failure. The opportunities to distinguish species dependent on the two markers are high for insects, amphibians, reptiles and birds with recognizable barcoding gaps, though *COI* appears to provide better species resolution after sequence alignment via BLAST, which might be a bias brought in by the reference databases available at this moment in Genbank (28). Furthermore, it will be more challenging to differentiate indigenous mammals using *COI* and *16S* because neither of them is capable to display a perfect species boundary according to our exploration. This might be a reason why until now fewer barcode records of *COI* and *16S* are accessible for mammals despite their prevalence in amphibians and reptiles. Nevertheless, it should be noted that the phylogenetic pattern reconstructed with *16S* through NJ algorithm seems more reliable than *COI*, providing a picture generally analogous to the conventional taxonomic classifications. In sum, we speculate that both mitochondrial *COI* and *16S* could function comparably at least as an eligible barcode marker for most species involved in current study, and that application of the two genetic markers relying on bioinformatic approaches should be cautious on a case-by-case basis.

In contrast to earlier studies, we realize high frequency of multiple sequences from one single PCR product as well as many *COI* haplotypes bearing non-sense mutations in our experimental setting. In fact, the heteroplasmy in mtDNA and the presence of nuclear pseudogenes of mitochondrial origin (*numts*) have raised many concerns in the field of barcoding (27). It is known that each eukaryotic cell could contain approximately 1000 copies of mtDNA, leading to a condition called heteroplasmy, where both wild-type and mutant mtDNA molecules

Table 3. *COI* sequences and haplotypes obtained from the same samples using two pairs of PCR primers.

COI PCR	Sample ID	Jungle_ fowl-B	Tibetan_ donkey3-B	Tibetan_ donkey5-B	Yunnan_ donkey8-B	Yunnan_ donkey9-B	Dezhou_ donkey4-B	Dezhou_ donkey52-S
1st pair	sequence #	2	3	6	2	9	1	13
	haplotype #	1	2	5	1	8	1	12
	translatable haplotype #	0	0	0	0	0	0	0
2nd pair	sequence #	4	4	2	3	3	6	8
	haplotype #	3	3	1	2	2	5	7
	translatable haplotype #	3	2	1	1	2	3	3

co-exist within the same cell (37). As illustrated by our data, insects, reptiles and mammals possess strong heteroplasmic phenomena in their mitochondrial genome while the mtDNAs of amphibians and birds hold fewer mutations (**Figure 8a**). We argue this difference is chiefly because of the properties of specimens sampled rather than due to the nature of the species since it has been demonstrated that the number of mtDNAs each mitochondrion carries is in a tissue-specific manner (38, 39). Yet interestingly, our findings unveil that the copy number of *COI* haplotypes is not tightly associated with that of *16S* from the same specimen (**Figure 8b**), implying that evolutions of the two mitochondrial fragments are not synchronous, undergoing a relatively independent pattern that might be controlled by their protein coding abilities.

Meanwhile it is very likely that nuclear *numts* are also co-amplified by using universal *COI* and *16S* primers. Due to the differences in genetic code between mitochondrial and nuclear genomes, *numts* are documented and recognized as non-functional copies of mtDNA with diverse sizes naturally integrated into the nuclear chromosome through unknown mechanism (40). Once inserted into nucleus, *numts* decelerate their evolutionary rate and become molecular fossils of mtDNA, which are thought to be indispensable for recovering ancient relationships (41, 42). When examining the translation of *COI* haplotypes, we uncover a big portion of non-coding pseudogenes with extremes that no translatable *COI* is identified from species like Jungle fowl (*Gallus gallus*) and donkeys (*Equus asinus*). Under such circumstance, it will be more reasonable to believe that these non-functional sequences are primarily derived from *numts* as extraction methods preferring nuclear DNA is conducted before. To ask whether PCR primers could revise this preference, we check the products amplified from another pair of *COI* primers (**Supplemental Table S2** *COI* 2nd pair) for Jungle fowl and donkeys. The same criteria are applied to guide TA cloning and Sanger sequencing for Jungle fowl and six donkeys, from which the highest or the lowest copy numbers of haplotype are detected with COI-C0 primers for each of the three breeds (Tibetan, Yunan and Dezhou Donkey). This time, the chance to gain functional sequence is improved, but no correlation of the copy numbers of *COI* haplotypes is observed from the two primer pairs, confirming these primers are picking up homologous sequences from distinct gene loci (**Table 3**).

On the other hand, in order to evaluate the potential misidentifications that could be caused by *numts* sequences, we decide to keep them in the analyses as outlined above. Our results show that coding *COI* in most cases allows methodological approaches to achieve more, but the influence of *numts* on the accuracy of taxonomic description is limited, suggesting that majority *numts* screened in this study are merely evolved for brief periods of time. Surprisingly, phylogenetic hierarchies deduced from both NJ and ML could position all *COI numts* to their expected places at the species level except for primates and Equus, which have been discussed earlier. More intriguingly, in-depth analysis in **Figure 6** classifies two groups of non-coding *numts* from Tibetan sheep, among which seven are clustered with functional *COI* haplotypes whereas the other three are separated as outgroup with a stronger discriminatory power, at least in ML phylogram, than their coding counterparts. Taken together, these observations indicate that it is indeed not easy to characterize the role of *numts* as it stands for an ongoing evolutionary procession (41). Of course, it certainly is unfair to treat sequences as *numts* solely based on translation, which is not feasible for *16S*. Yet it should be acceptable considering that the percentages of novel sequences are parallel among translatable *COI*, *16S* and COI peptides but not non-coding *COI* (**Figure 3b**). In a word, our preliminary findings recommend that a careful investigation of *numts* may provide novel insights into the DNA barcoding system with potentially widespread scientific and practical benefits.

Acknowledgement
We sincerely appreciate Dr. Yanfen Cheng and Wenjia Huang at Nanjing Agricultural University for the sample collection. This work is funded by the National Key R&D Program of China (2018YFC1200201).

Conflict of interest
The authors declare that there is no conflict of interests regarding the publication of this paper.

Supplementary Information
The supplemental material can be downloaded online at:
https://stemedicine.org/index.php/stem/article/view/95

References

1. Liu J, Ouyang Z, Pimm SL, Raven PH, Wang X, Miao H, et al. Protecting China's Biodiversity. Science. 2003, 300:1240-1.
2. He J, Yan C, Marcel H, Wan X, Ren G, Hou Y, et al. Quantifying the effects of climate and anthropogenic change on regional species loss in China. PLoS One. 2018, 13(7):e0199735.
3. Zheng HR, Cao S. Threats to China's biodiversity by contradictions policy. Ambio. 2015, 44(1):23-33.
4. Daugherty CH, Cree A, Hay JM, Thompson MB. Neglected taxonomy and continuing extinctions of tuatara (Sphenodon). Nature. 1990, 347(6289):177-9.
5. Brisson, J. Aphid wing dimorphisms: linking environmental and genetic control of trait variation. Philos Trans R Soc Lond B Biol Sci. 2010, 365(1540):605-16.
6. Kreuzer M, Howard C, Adhikari B, Pendry CA, Hawkins JA. Phylogenomic approaches to DNA barcoding of herbal medicines: developing clade-specific diagnostic characters for berberis. Front Plant Sci. 2019, 10:586.
7. JMurugaiyan J, Roesler U. MALDI-TOF MS profiling-advances in species identification of pests, parasites, and vectors. Front Cell Infect Microbiol. 2017, 7:184.
8. Hebert P, Cywinska A. Biological identifications through DNA barcodes. Proc Biol Sci. 2003, 270(1512):313-21.
9. Savolainen V, Cowan RS, Vogler AP, Roderick GK, Lane R. Towards writing the encyclopaedia of life: an introduction to DNA barcoding. Philos Trans R Soc Lond B Biol Sci. 2005, 360(1462):1805-11.
10. Haji Bab Aei M, Singer G, Hebert P, Hickey DA. DNA barcoding: how it complements taxonomy, molecular phylogenetics and population genetics. Trends Genet. 2007, 23(4):167-72.
11. Matilainen O, Quirós P, Auwerx J. Mitochondria and epigenetics – crosstalk in homeostasis and stress. Trends Cell Biol. 2017, 27(6):453-63.
12. Akhmedov AT, Marín-García J. Mitochondrial DNA maintenance: an appraisal. Mol Cell Biochem. 2015, 409(1):283-305.
13. Vences M, Thomas M, Arie V, Chiari Y, Vieites DR. Comparative performance of the 16S rRNA gene in DNA barcoding of amphibians. Front Zool. 2005, 2(1):5.
14. Hebert PD, Ratnasingham S, deWaard JR. Barcoding animal life: cytochrome c oxidase subunit 1 divergences among closely related species. Proc Biol Sci. 2003;270 Suppl 1(Suppl 1):S96-9.
15. Ratnasingham S, Hebert PD. bold: The Barcode of Life Data System (http://www.barcodinglife.org). Mol Ecol Notes. 2007;7(3):355-64.
16. Yang C, Xiao Z, Zou Y, Zhang X, Yang B, Hao Y, et al. DNA barcoding revises a misidentification on musk deer. Mitochondrial DNA. 2015;26(4):605-12.
17. Che J, Chen HM, Yang JX, Jin JQ, Jiang KE, Yuan ZY, et al. Universal COI primers for DNA barcoding amphibians. Mol Ecol Resour. 2012, 12(2):247-58.
18. Van D, Ranjit K, Morrow CD, Blanchard EE, Taylor CM, Martin DH, et al. In silico and experimental evaluation of primer sets for species-level resolution of the vaginal microbiota using 16S ribosomal RNA gene sequencing. J Infect Dis. 2019, 219(2):305-14.
19. Elbrecht V, Taberlet P, Dejean T, Valentini A, Usseglio-Polatera P, Beisel JN, et al. Testing the potential of a ribosomal 16S marker for DNA metabarcoding of insects. PeerJ. 2016, 4:e1966.
20. Astrin JJ, Huber B, Misof B, Klütsch CFC. Molecular taxonomy in pholcid spiders (Pholcidae, Araneae): evaluation of species identification methods using CO1 and 16S rRNA. Zool Scr. 2006;35(5).
21. Schmitteckert EM, Prokop CM, Hedrich HJJLA. DNA detection in hair of transgenic mice-a simple technique minimizing the distress on the animals. Lab Anim. 1999, 33(4):385.
22. Berner DK, Cavin C, Erper I, Tunali B. First report of anthracnose of mile-a-minute (*Persicaria perfoliata*) caused by colletotrichum cf. gloeosporioides in Turkey. Plant Dis. 2012, 96(10):1578.
23. Srivathsan A, Meier R. On the inappropriate use of Kimura-2-parameter (K2P) divergences in the DNA-barcoding literature. Cladistics. 2012, 28:190-194.
24. Clare EL, Kerr K, KönigslöW T, Wilson JJ, Hebert PDN. Diagnosing mitochondrial DNA diversity: applications of a sentinel gene approach. J Mol Evol. 2008, 66(4):362-7.
25. Min XJ, Hickey DA. DNA barcodes provide a quick preview of mitochondrial genome composition. PLoS One. 2007;2(3):e325.
26. Zhang AB, Feng J, Ward RD, Wan P, Gao Q, Wu J, et al. A new method for species identification via protein-coding and non-coding DNA barcodes by combining machine learning with bioinformatic methods. PLoS One. 2012;7(2):e30986.
27. Austerlitz F, David O, Schaef Fe R B, Bleakley K, Olteanu M, Leblois R, et al. DNA barcode analysis: a comparison of phylogenetic and statistical classification methods. BMC Bioinformatics. 2009, 10 Suppl 14(Suppl 14):S10.
28. Meyer CP, Paulay G. DNA barcoding: error rates based on comprehensive sampling. PLoS Biol. 2005, 3(12):e422.
29. Fišer Pečnikar Ž, Buzan EV. 20 years since the introduction of DNA barcoding: from theory to application. J Appl Genet. 2013;55(1):43-52.
30. Song H, Buhay JE, Whiting MF, Crandall KA. Many species in one: DNA barcoding overestimates the number of species when nuclear mitochondrial pseudogenes are coamplified. Proc Natl Acad Sci U S A. 2008, 105(36):13486-91.
31. Thalmann O, Hebler J, Poinar HN, Pääbo S, Vigilant L. Unreliable mtDNA data due to nuclear insertions: a cautionary tale from analysis of humans and other great apes. Mol Ecol. 2004, 13(2):321-35.
32. Turvey ST, Marr MM, Barnes I, Brace S, Tapley B, Murphy RW, et al. Historical museum collections clarify the evolutionary history of cryptic species radiation in the world's largest amphibians. Ecol Evol. 2019, 9(18):10070-84.
33. Kress WJ, Erickson DL. DNA barcodes: methods and protocols. Methods Mol Biol. 2012, 858:3-8.
34. Varadharajan B, Parani M. DMSO and betaine significantly enhance the PCR amplification of ITS2 DNA barcodes from plants. Genome. 2021;64(3):165-71.
35. Moritz C, Dowling TE, Brown WM. Evolution of animal mitochondrial DNA: relevance for population biology and systematics. Annu Rev Ecol Syst. 1987, 18(1):269-92.
36. White DJ, Wolff JN, Pierson M, Gemmell NJ. Revealing the hidden complexities of mtDNA inheritance. Mol Ecol. 2008, 17(23):4925-42.
37. Lightowlers RN, Chinnery PF, Turnbull DM, Howell N. Mammalian mitochondrial genetics: heredity, heteroplasmy and disease. Trends Genet. 1997, 13(11):450-5.
38. Jenuth JP, Peterson AC, Shoubridge EA. Tissue-specific selection for different mtDNA genotypes in heteroplasmic mice. Nat Genet. 1997, 16(1):93-5.
39. Li M, SchröDer R, Ni S, Madea B, Stoneking M. Extensive tissue-related and allele-related mtDNA heteroplasmy suggests positive selection for somatic mutations. Proc Natl Acad Sci U S A. 2015, 112(8):2491-6.
40. Berg OG, Kurland CG. Why mitochondrial genes are most often found in nuclei. Mol Biol Evol. 2000;17(6):951-61.
41. Bensasson D, Zhang DX, Hartl DL, Hewitt GM. Mitochondrial pseudogenes: evolution's misplaced witnesses. Trends Ecol Evol. 2001, 16(6):314-21.
42. Ricardo PC, Franoso E, Arias MC. Mitochondrial DNA intra-individual variation in a bumblebee species: A challenge for evolutionary studies and molecular identification. Mitochondrion. 2020, 53:243-54.